

Molecular Disks in the Elliptical Galaxies NGC 83 and NGC 2320

L. M. Young

Physics Department, New Mexico Institute of Mining and Technology, Socorro, NM 87801

lyoung@physics.nmt.edu

ABSTRACT

The molecular gas in (some) early type galaxies holds important clues to the history and the future of these galaxies. In pursuit of these clues we have used the BIMA millimeter array to map CO emission in the giant elliptical galaxies NGC 83 and NGC 2320 and to search for CO emission from the S0 galaxy NGC 5838. We also present *V* and *R* images of NGC 83 and NGC 2320 which trace their dust distributions and enable a search for disky stellar structures. The molecular gas in NGC 83 is well relaxed, but both CO and dust in NGC 2320 show asymmetric structures which may be linked to a recent acquisition of the gas. However, the specific angular momentum distribution of molecular gas in NGC 2320 is consistent with that of the stars. Internal origin of the gas (stellar mass loss) cannot, therefore, be ruled out on angular momentum grounds alone. We also consider the evidence for star formation activity and disk growth in these two elliptical galaxies. Radio continuum and FIR fluxes of NGC 83 suggest star formation activity. NGC 2320 has bright [O III] emission, but its large radio/FIR flux ratio and the mismatch between the kinematics of CO and [O III] suggest that the ionized gas should not be attributed to star formation. The origin and future of these two CO-rich early type galaxies are thus complex, multi-faceted stories.

Subject headings: galaxies: elliptical and lenticular, cD — galaxies: ISM — galaxies: kinematics and dynamics — galaxies: individual (NGC 83, NGC 2320, NGC 5838)

1. Introduction

Since the time of IRAS it has been known that a significant number — perhaps 50%— of early type (E and S0) galaxies have detectable far-IR emission in the $60\mu\text{m}$ and $100\mu\text{m}$ bands (Knapp, Guhathakurta, Kim, & Jura 1989). The galaxies which are FIR-bright sometimes also have molecular gas; for example, Knapp & Rupen (1996) quote CO detection rates of 20 to 80% for ellipticals which are brighter than 1 Jy at $100\mu\text{m}$. Thus some of the galaxies which are *supposed* to be poor in cold gas are not, which raises a variety of interesting issues. In spiral galaxies, for example, we are accustomed to thinking of very intimate connections between the stellar disks and the cold gas. What about the early type galaxies which are rich in cold gas — what (if any) is the

connection between their stars and their gas? Where did this cold gas come from, and how does it evolve?

The CO-rich early type galaxies could have acquired their cold gas from external sources (including accretion and major mergers) or from internal stellar mass loss. The latter source is plausible in the sense that the rates of mass return to the interstellar medium over 10 Gyr are more than adequate to account for the observed cold gas masses (Faber & Gallagher 1976; Ciotti et al. 1991; Brighenti & Mathews 1997). After all, the molecular gas masses are still typically much smaller, per unit optical luminosity, than for spirals (Lees et al. 1991), so that the CO-rich early type galaxies are only rich in comparison to other early types. However, if the molecular gas has an internal origin, one might expect to find a trend of increasing CO mass in galaxies of higher optical luminosity. Such trends are not observed. Most authors then suggest that the cold gas in early type galaxies must have been acquired from outside or as a leftover from a major merger (Knapp & Rupen 1996; Lees et al. 1991). Therefore, the relatively few early type galaxies which do have molecular gas could hold vital clues to the evolution of the early types.

Beyond simply noting the molecular gas content of early type galaxies, observations which resolve the *distribution and kinematics* of the gas are crucial for understanding its origin and future. For example, gas which originated in stellar mass loss must have a specific angular momentum distribution which is consistent with that of the stars. Such gas may have somewhat less angular momentum than the stars do, but it should certainly not be misaligned or counterrotating. In this way the comparison of stellar and cold gas kinematics can help to clarify the origin of the gas. In addition, molecular gas is the raw material for star formation; the properties of the molecular gas determine where and how star formation may happen. The semi-analytic simulations of Khochfar & Burkert (2004) suggest that a few tens of percent of all disk ellipticals could have grown their stellar disks out of cold gas accreted from the intergalactic medium. A better understanding of the molecular gas in early type galaxies could provide evidence either for or against this disk growth scenario.

The distribution and kinematics of the molecular gas are also valuable for mass modelling. The dissipational nature of the cold gas means that the shapes of the gas orbits are much better known than are the shapes of the stellar orbits (de Zeeuw & Franx 1989; Cretton, Rix, & de Zeeuw 2000). Gas kinematics can be used to infer the galaxy potential in a way which is more robust than, or at least complementary to, what one can do with stellar kinematics.

There are now around a dozen elliptical or possible elliptical galaxies in the literature with high quality CO maps which resolve their molecular distributions (Inoue et al. 1996; Young 2002; Okuda et al. 2005; Rupen 1997; Wiklind, Combes, Henkel, & Wyrowski 1997). (The phrase “possible ellipticals” is used here because of the well-known difficulty in separating ellipticals from S0s, especially for photographic material. Two merger remnants with $r^{1/4}$ structure are also counted.) Most have molecular gas in a rotating disk of radius ~ 1 to a few kpc in radius. These radii are comparable to the effective or half-light radii r_e . The molecular masses are about $10^9 M_\odot$. Young

(2002) shows that such molecular disks could build dynamically cold stellar disks similar those found in disk ellipticals. The unusual ellipticals Cen A (NGC 5128) and Perseus A (NGC 1275) have molecular gas associated with shells (Charmandaris, Combes, & van der Hulst 2000) and H α filaments (Hatch et al. 2005), but these are the only ellipticals known to have molecular gas at such large radii. Thus, the study of the distribution and kinematics of molecular gas in early type galaxies is really just beginning.

This paper presents new CO maps which resolve the distribution and kinematics of molecular gas in NGC 83 and NGC 2320, which are now two of the most luminous early type galaxies with such maps. A deep search for CO emission from NGC 5838 is also presented. Broadband optical images of NGC 83 and NGC 2320 reveal the dust distributions and optical structure of these galaxies, and we discuss correlations between dust, CO, and stellar structures. We also present comparisons of stellar, molecular, and ionized gas kinematics in NGC 2320; the cumulative specific angular momentum distributions of molecular gas and stars help to reveal the origin of the cold gas.

We find some evidence for both an internal origin (stellar mass loss) and an external origin of the molecular gas in NGC 83 and NGC 2320. The gas/dust disk in NGC 83 is very well relaxed though the gas in NGC 2320 shows some strong asymmetries which should shear away on quite short timescales. The specific angular momentum distribution of the molecular gas in NGC 2320 may be consistent with an internal origin, however. Evidence for star formation activity and disk growth is also mixed. The radio/FIR flux ratio in NGC 2320 suggests that the galaxy has relatively little star formation activity; it is bright in [O III] emission, but the kinematics of [O III] do not match those of the molecular gas. In short, it is clearly too early to regard the origin and the future of the CO-rich early type galaxies as a mystery solved, but the new CO maps of NGC 83 and NGC 2320 surely provide important clues to an emerging picture.

2. Selection and properties of the galaxies

NGC 83, NGC 2320, and NGC 5838 were selected for CO mapping because they are early type galaxies with relatively strong CO detections in the single-dish surveys of Wiklind, Combes, & Henkel (1995) [WCH95] and Knapp & Rupen (1996). Both of those surveys observed morphological ellipticals with IRAS 100 μ m fluxes $S_{100\mu\text{m}} > 1.0$ Jy. (Many of the morphological classifications have not been checked with modern CCD images.) WCH95 detected CO emission in 16 of the 29 elliptical galaxies they searched. Their 7 strongest CO detections in the northern hemisphere were mapped previously (Young 2002), and NGC 83 and NGC 2320 are two of the next brightest. Knapp & Rupen (1996) detected CO emission in 11 of 42 early type galaxies, and NGC 5838 has one of the largest fluxes in that sample.

NGC 2320 and NGC 5838 were also selected because of the opportunity to compare the kinematics of cold gas and stars in early-type galaxies. Longslit stellar and ionized gas kinematics are

available for multiple position angles in NGC 2320 from the work of Cretton, Rix, & de Zeeuw (2000). Furthermore, both NGC 2320 and NGC 5838 have been mapped in the SAURON survey of early type galaxies (de Zeeuw et al. 2002), so that full two-dimensional maps of stellar line-of-sight velocity profiles, ionized gas kinematics and line strength indices will be available for the inner parts of these galaxies. The claimed CO detection in NGC 5838 has not been confirmed, but we are still able to compare stellar and gas kinematics for NGC 2320.

Table 1 gives some properties of the three galaxies which are studied in this paper. The available data indicate that NGC 83 and NGC 2320 are luminous ellipticals whose structure and stellar populations are typical of their class. Kuntschner et al. (2001) show that H β and $\langle \text{Fe} \rangle$ absorption in NGC 2320 are consistent with solar metallicity and a large luminosity-weighted mean age. NGC 2320 does, however, have the strongest [O III] emission in the sample of Kuntschner et al. (2001). H β and Mg₂ indices for NGC 83 are also typical of the early type galaxies in the sample of Trager et al. (1998). WCH95 consider NGC 83 to be a member of a poor group of mostly early type galaxies and NGC 2320 to be a member of the cluster Abell 569.

NGC 5838 is a well-studied S0 galaxy with a thick nuclear dust ring (Ravindranath et al. 2001; Peletier et al. 1999). It also contains a nuclear kinematically decoupled region which has the same colors as the rest of the bulge (Falcón-Barroso et al. 2003). The large scale structure is discussed at greater length by Sandage & Bedke (1994), and Michard & Marchal (1994) suggest that the outer disk may show faint signs of a spiral pattern. In the SAURON sample of early-type galaxies (de Zeeuw et al. 2002), NGC 5838 is classed as a field lenticular.

3. Observations and data analysis

3.1. Optical imaging of NGC 83 and NGC 2320

Since NGC 83 and NGC 2320 are two of the most unusually CO-rich early type galaxies, and since their morphology has been rather meagerly studied in the past, it is worthwhile to reinvestigate their structure with high quality optical images. Early type galaxies sometimes contain surprises (Donzelli & Davoust 2003). Broadband V and R images of NGC 83 and NGC 2320 were obtained by L. van Zee in November 2002 with MiniMo on the WIYN 3.5m telescope under non-photometric conditions.¹ The total exposure time was 1260 sec in V and 900 sec in R ; the pixel scale (after binning) is 0.28'' pix⁻¹, the field of view is 10', though the galaxies are not centered in the field, and the seeing was 1.0'' – 1.2''. The images were processed in the standard manner for overscan, bias, flat field and illumination correction, then combined. Additional data processing details may be found in van Zee, Barton, & Skillman (2004).

¹The WIYN Observatory is a joint facility of the University of Wisconsin-Madison, Indiana University, Yale University, and the National Optical Astronomy Observatories.

For comparison to radio data, sky coordinates were obtained from 6 to 12 stars in the POSS II digitized sky survey images, and the optical images were rotated to have north up. CO images were regridded to match the coordinate system in optical images. Dust images were constructed by first convolving the V images to match the resolution of the R images and then dividing the two. After careful masking of stars, galaxy isophotes were fit using the ELLIPSE task inside the STSDAS package. Ellipse fits were performed on both R and V images independently. These fitted isophotes also give surface brightness profiles which were fit to a Sersic function (Ciotti & Bertin 1999):

$$\mu(R) = \mu_0 + \frac{2.5 b}{\ln 10} (R/R_e)^{1/m}.$$

Sersic fits used the ellipse semimajor axis as the independent variable (rather than the geometric mean axis).

3.2. CO data

NGC 83, NGC 2320 and NGC 5838 were observed in the ^{12}CO $J = 1 \rightarrow 0$ line with the 10-element Berkeley-Illinois-Maryland Association (BIMA) millimeter interferometer at Hat Creek, CA (Welch et al. 1996). These observations were carried out in the C configuration (projected baselines 3 to 34 $\text{k}\lambda$) between October 2002 and December 2002. Four tracks of data were obtained for each galaxy with a single pointing centered on the optical position. Each observation covered a velocity range of 1300 to 1400 km s^{-1} centered on the single-dish CO velocity, and these data have sensitivity to structures from point sources up to objects 60–80'' in diameter. System temperatures were mostly in the 200–400 K range, with the exception that three of the tracks on NGC 5838 had system temperatures ranging from 400 to 600 K. Table 2 summarizes important parameters of these observations.

Reduction of the BIMA data was carried out using standard tasks in the MIRIAD package (Sault, Teuben, & Wright 1995). Electrical line length calibration was applied to the tracks on NGC 5838, which were taken after the array switched from coaxial cable to optical fiber; for NGC 83 and NGC 2320 it was not needed. One of the tracks on NGC 5838 was also explicitly corrected for amplitude decorrelation on longer baselines using data from an atmospheric phase monitor and the MIRIAD task *uvdecor* (Lay 1999; Akeson 1998; Regan et al. 2001; Wong 2001). The atmospheric decorrelation is estimated using a small interferometer with a fixed 100 meter baseline which measures the rms path length difference in the signal from a commercial broadcast satellite. This corrected track had rms path lengths in the range of 200 to 300 microns, and the median amplitude correction factor was 3%. The remainder of the tracks were taken in stabler weather and were not explicitly corrected for decorrelation because normal amplitude calibration can take out most of the effect (Wong 2001).

Absolute flux calibration was based on observations of Uranus or Mars. When suitable planets were not available, the secondary calibrator 3C454.3 was used as it is usually monitored several

times per month. Phase drifts as a function of time were corrected by means of a nearby calibrator observed every 30 to 40 minutes. Gain variations as a function of frequency were corrected by the online passband calibration system; inspection of data for 3C273 indicate that residual passband variations are on the order of 10% or less in amplitude and 2° in phase across the entire band.

The calibrated visibility data were weighted by the inverse square of the system temperature and the inverse square of the amplitude decorrelation correction factor (if used), then Fourier transformed. NGC 83 and NGC 2320 showed some line emission; the dirty images were lightly deconvolved with the Clark clean algorithm, as appropriate for these compact, rather low signal-to-noise detections. (No continuum subtraction was needed for these galaxies.) Integrated intensity and velocity field maps were produced by the masking method: the deconvolved image cube was smoothed along both spatial and velocity axes, and the smoothed cube was clipped at about 2.5σ in absolute value. The clipped version of the cube was used as a mask to define a three-dimensional volume in which the emission is integrated over velocity (Wong 2001; Regan et al. 2001). Continuum images were made by averaging all of the line-free channels in the final spectral line cubes. Table 2 gives 3σ limits for point source continuum emission at the centers of the galaxies; Table 3 gives beam size and sensitivity information for the final spectral line cubes.

4. Results

4.1. NGC 83: optical morphology

Over a radial range of $6''$ to at least $80''$ (exterior to a dusty region described below), the surface brightness profile of NGC 83 is very well described by a $r^{1/4}$ profile (Figure 1). In fact, Sersic fits give fitted values of the shape parameter m between 4.1 and 5.1 for reasonable radius ranges. A value of $m = 4$ would correspond exactly to a $r^{1/4}$ profile. Formal uncertainties in the fitted value of m are on the order of 0.07, but it is clear that the range of values indicated above is a better indicator of the true uncertainty.

The galaxy's position angle remains constant at -66° over $6''$ to $30''$ (Figure 2). The ellipticity of the isophotes is also flat at a mean value of $\epsilon = 0.085$ over this radius range, and the isophotes show no significant deviation from pure ellipses. From $30''$ outwards, the structure of the galaxy is somewhat more complicated; a slight “wing” or knee in the surface brightness at $30\text{--}42''$ (and probably some scattered light from a trio of bright stars) are responsible for excursions in ellipticity, position angle, and the Fourier components a_3 and a_4 . Thus, the surface brightness profile of NGC 83 is entirely consistent with its classification as an elliptical, and the interior is neither boxy nor disk-like with no position angle twist.

The $V - R$ dust image (Figure 3) shows a very regular, relaxed disk of semimajor axis $\sim 5''$ which is well aligned with the optical major axis. The northeast side of the disk shows somewhat stronger reddening and must be the near side. The axis ratio of the dust disk is estimated in the

range $b/a = 0.8$ to 0.9 , implying that the inclination of the disk is between 26° and 37° . The stellar body of the galaxy is just marginally rounder than the dust disk, and there is no evidence for dust lanes beyond this central disk. The color image also shows that the nucleus is bluer than the rest of the galaxy.

4.2. NGC 2320: optical morphology

The optical morphology of NGC 2320 is also consistent with its classification as elliptical, though its structure is more complicated than that of NGC 83. Over semimajor axes $14''$ to $90''$ (there is dust absorption interior to $12''$), its surface brightness is well described by a $r^{1/4}$ profile (Figure 4). The fitted Sersic shape parameters fall in the range $m = 4.0$ to 5.2 for reasonable radius ranges. The position angle is consistent with a constant value (no twists) of -38° from $14''$ to $70''$ (Figure 5). A bright annulus of semimajor axis $15''$ shows up as a small bump in the surface brightness profile and a prominent peak in ellipticity. Just interior to the bright annulus the isophotes are strongly boxy ($a_4/a \sim -0.02$ near semimajor axis of $10''$) but the bright annulus itself shows $a_4/a \sim 0$. Beyond $30''$ we find a constant ellipticity $\epsilon = 0.3$ and a gradual transition from $a_4/a = -0.01$ (boxy) at $30''$ to $a_4/a \sim +0.02$ (disky) at $70''$. These results agree reasonably well with those of Nieto et al. (1991) if the scaling on the semimajor axis of their Figure 2.14 is off by about a factor of two, though we do not confirm the position angle drift claimed by those authors.

The $V - R$ image (Figure 6) shows significant reddening by dust within $12''$ of the nucleus. The northeast side of the disk is the near side. The bilateral symmetry of the molecular gas distribution (Section 4.6) makes it clear that the far (southwest) side of the disk is also present, although it is not obvious from the reddening alone. The dust is also reflection-symmetric about the minor axis out to a semimajor axis of $10''$; beyond $10''$ there is some “extra” absorption southeast of the nucleus. The symmetric part of the dust disk has an axis ratio $b/a = 0.58$ which corresponds to an inclination of 55° . Cretton, Rix, & de Zeeuw (2000) also see this dust feature in residuals to a multi-Gaussian fit of their V-band image and estimate its axis ratio to be 0.5 ($i = 60^\circ$) or 0.32 ($i = 71^\circ$) after unsharp masking. An inclination of 60° is therefore adopted for the gas and dust disk.

4.3. CO in NGC 5838

NGC 5838 is not detected in CO emission. The H₂ column density limits in Table 3 correspond to a mass limit $M(H_2) < 5 \times 10^6 M_\odot$ for an unresolved source at the center of the field of view. (The adopted H₂/CO conversion factor is discussed in Section 4.4.) This upper limit is well below the expected CO mass based on the work of Knapp & Rupen (1996), whose CO $J = 2 \rightarrow 1$ spectrum shows a peak brightness temperature (T_{mb}) of about 10 mK and an rms noise level of 5.4 mK per 10 km s⁻¹ channel. The shape is reminiscent of a two-horned spectrum from a rotating disk, with the

optical velocity roughly midway between two peaks. Our BIMA observations achieved an rms noise level of $17 \text{ mJy beam}^{-1} = 14 \text{ mK}$ in a data cube with 40 km s^{-1} channels and an $11 \times 10''$ beam. If the $J = 2 \rightarrow 1$ and $J = 1 \rightarrow 0$ transitions have the same excitation temperature (Lees et al. 1991) and if the CO emission were still unresolved in the smaller BIMA beam, its brightness temperature would rise to 90 mK. We would therefore have expected to detect it at a signal-to-noise ratio of 6 in three or four independent channels on each “horn”. Clearly, we did not detect emission from NGC 5838 at those levels.

Of course, if the emission in NGC 5838 is extended on the $30''$ scales probed by CSO it would still be 10 mK bright at the higher resolution and our BIMA data would not detect it, but the dust distribution suggests that this is probably not the case. The dust disk which shows up prominently in the HST image of Ravindranath et al. (2001) has a semimajor axis $< 4''$. Thus, if the CO were associated with dust as it is in NGC 83 and NGC 2320 (Sections 4.5 and 4.6) it would be well matched to the BIMA beam size and bright enough to detect with the interferometer.

Our present nondetection of CO $J = 1 \rightarrow 0$ emission from NGC 5838 is also consistent with a recent nondetection at the IRAM 30m telescope (Combes et al. 2005). Thus, we infer that the CSO spectrum might simply show an unfortunate baseline ripple with an amplitude of about 3 mK (smaller than the rms noise level of those data) and a period of 230 MHz (300 km s^{-1}).

4.4. NGC 83 and NGC 2320: CO fluxes and H_2 masses

Total CO fluxes for NGC 83 and NGC 2320 were measured from the integrated intensity images; their uncertainties are probably 15%, with approximately equal contributions coming from the absolute calibration and from uncertainties in choosing the spatial region to be summed. H_2 masses are calculated using the distances in Table 1 and a “standard” H_2/CO conversion factor of $3.0 \times 10^{20} \text{ cm}^{-2} (\text{K km s}^{-1})^{-1}$ as in WCH95. With this conversion factor, H_2 masses are related to CO fluxes S_{CO} by $M(\text{H}_2) = (1.22 \times 10^4 M_{\odot}) D^2 S_{\text{CO}}$ where D is the distance in Mpc and S_{CO} is the CO flux in Jy km s^{-1} . No correction has been made for the presence of helium except where noted.

The interferometric CO flux for NGC 83, $22 \pm 3 \text{ Jy km s}^{-1}$, agrees very well with the single dish flux measured by WCH95. The IRAM 30m telescope detected a total flux of 4.7 K km s^{-1} (on the T_{mb} scale), which corresponds to $21.8 \text{ Jy km s}^{-1}$ at 4.64 Jy/K (Guelin, Kramer, & Wild 1995). The uncertainty in the single dish CO flux is roughly 10% for absolute calibration, 10% for statistical uncertainty, and another 5% from estimating the baseline level—in short, the two measurements are consistent within their errors. The molecular mass of NGC 83 is therefore $(2.0 \pm 0.3) \times 10^9 M_{\odot}$. The BIMA CO spectrum (Figure 7) also shows close agreement with the center velocity and width found by WCH95 and with the optical velocity from Huchra et al (1999).

Our new CO flux for NGC 2320, $56 \pm 8 \text{ Jy km s}^{-1}$, is more than five times larger than the total flux given in WCH95 (10 Jy km s^{-1}). However, it is clear that the discrepancy is caused by the

galaxy's large line width. Our BIMA data show emission over a range of $\approx 830 \text{ km s}^{-1}$ (Section 4.6). WCH95 claimed a line width of only 320 km s^{-1} ; in fact, they only detected one end of the line, the full 830 km s^{-1} line being difficult to distinguish from low level baseline variations in a single dish spectrum. The total molecular mass of NGC 2320 is thus $(4.3 \pm 0.6) \times 10^9 M_\odot$. Our new systemic velocity of $5886 \pm 20 \text{ km s}^{-1}$ is also in better agreement with the optical velocity measurements of $5944 \pm 15 \text{ km s}^{-1}$ (Smith et al 2000) and $5725 \pm 60 \text{ km s}^{-1}$ (de Vaucouleurs et al. 1991). Figure 8 shows the integrated CO spectrum of NGC 2320.

4.5. NGC 83: CO distribution and kinematics

The distribution and kinematics of CO in NGC 83 are (as best we can tell for this rather limited resolution) entirely consistent with a symmetric, relaxed disk in dynamical equilibrium. A fit of a two-dimensional Gaussian to the integrated intensity image of Figure 9 gives a deconvolved FWHM of $5.3 \times 4.4''$ at a position angle of 47° (i.e. elongated on the optical *minor axis*), but since that deconvolved size is so similar to the angular resolution it is more instructive to look at the distribution in the individual channel maps (Figure 10). At the extreme channels (6047 km s^{-1} and 6464 km s^{-1}) the centroids of the emission are displaced towards opposite ends of the major axis of the dust disk, and in the interior channels the emission is elongated along the minor axis of the dust disk. Thus, the kinematic major axis of the CO is clearly aligned with the major axis of the dust disk and with the galaxy itself.

CO emission does not appear to extend beyond the dust disk, and indeed the evidence suggests that the CO emission is exactly coincident with the dust disk. The dust disk has a major axis diameter of about $10''$; thus, the CO radial extent along the major axis is most likely $5''$. Burstein et al. (1987) quote an effective radius $r_e = 27''$, so the CO/dust disk extends to $0.19 r_e$.

The kinematic center and inclination cannot be determined from the CO data alone, but the direction of the kinematic major axis and the product $V \sin(i)$ are well constrained. A fit of the CO velocity field (intensity-weighted mean velocity) with a solid body rotation curve gives the kinematic position angle to be $-64 \pm 1^\circ$ to the approaching major axis. (This formal error estimate is certainly smaller than the true uncertainty, due to the relatively poor resolution.) Thus, the kinematic position angle agrees well with the value adopted for the optical major axis, -66° . A major axis position-velocity slice is shown in Figure 11. The circular velocity $V_{\text{circ}} \sin(i)$ is estimated from the extreme channels which show emission (Figures 7 and 10). Since the global profile's edges are sharp compared to the 40 km s^{-1} channel width, we can very roughly account for instrumental broadening and local dispersion by taking the full width to be the difference in center velocities of those end channels. Such corrections are discussed in greater detail by Lavezzi & Dickey (1998b), for example. Thus the full width of the CO emission is $417 \text{ km s}^{-1} \pm 20 \text{ km s}^{-1}$, or $V_{\text{circ}} \sin(i) = 209 \text{ km s}^{-1}$.

Dynamical mass estimates for the center of NGC 83 are in agreement with expectations. If

the inclination of the dust disk (26° to 37°) is also adopted for the gas disk, we estimate V_{circ} to be between 350 km s^{-1} and 480 km s^{-1} at $5'' = 2.1 \text{ kpc}$. (The true maximum circular velocity might, of course, be larger than this if the turnover in the rotation curve is beyond the edge of the molecular disk.) The orbital timescale at the outer edge of the CO disk is then $3 \times 10^7 - 4 \times 10^7 \text{ yr}$. These velocities imply dynamical masses between $5.9 \times 10^{10} \text{ M}_\odot$ and $1.1 \times 10^{11} \text{ M}_\odot$ interior to 2.1 kpc , or $M_{gas}/M_{dyn} = 0.024 - 0.046$ including a factor of 1.36 for helium. Approximately 10% of the galaxy's light should originate at $r \leq 0.19 r_e$; for example, in a Dehnen (1993) model with $\gamma = 3/2$, 8.4% of the stellar mass is interior to $0.19 r_e$. NGC 83's absolute magnitude $M_V = -22.1$ then implies that the stellar luminosity interior to $0.19 r_e$ is $L_V = 5.1 \times 10^9 \text{ L}_\odot$, and in that region $(M/L)_V = 11 - 22$. This mass-to-light ratio is very similar to what Cretton, Rix, & de Zeeuw (2000) found for the center of NGC 2320.

4.6. NGC 2320: CO distribution and kinematics

4.6.1. The CO disk

In contrast to the symmetry and relaxed appearance of the CO in NGC 83, the molecular gas in NGC 2320 is quite asymmetric. The spectrum in Figure 8 shows that the flux density is twice as large on the high velocity side of the line as on the low velocity side. From the integrated intensity image (Figure 12) it is evident that the “extra” gas on the high velocity side is extended along the optical major axis toward the southeast; it contributes roughly 25% of the total CO flux of the galaxy, and it is coincident with the irregular dust lane just beyond the southeast end of the dust/gas disk (Figure 6). This extended CO emission is prominent in the channel maps (Figures 13 and 13) at velocities $\sim 6240 \text{ km s}^{-1}$, $10''$ southeast of the galaxy center. Channels at 5450 km s^{-1} and 6282 km s^{-1} show that the CO emission extends to a radius of $4''$ ($0.1 r_e$) on the northwest side of the nucleus and $10''$ ($0.2 r_e$) on the southeast side.

As was the case for NGC 83, the modest resolution does not allow us to determine the inclination of the gas disk independently from its rotation velocity. However, tilted-ring fits to the velocity field do constrain the major axis position angle to be $-36^\circ \pm 4^\circ$, where the quoted uncertainty is estimated from the dispersion among fits with slightly different radial ranges, initial conditions and weight schemes. Again, the kinematic major axis is consistent with the optical morphological major axis (-38°) though misalignments on the order of a few degrees cannot be ruled out.

Figure 14 shows a major axis position-velocity diagram for the CO emission from NGC 2320. The full width of the CO line is measured from the extreme channels which show emission, approximately corrected for turbulent and instrumental broadening as described in Section 4.5; it is $830 \text{ km s}^{-1} \pm 40 \text{ km s}^{-1}$, so $V \sin(i) = 415 \text{ km s}^{-1}$. Adopting an inclination of 60° from the dust disk (Section 4.2 and Cretton, Rix, & de Zeeuw (2000)) gives an estimated circular velocity 480 km s^{-1} at radii $4-10''$. The dynamical mass within $10''$ (3.8 kpc) is $2.0 \times 10^{11} \text{ M}_\odot$, so $M_{gas}/M_{dyn} = 0.030$ when helium is included.

4.6.2. Molecular gas vs. ionized gas

Figure 14 also compares CO kinematics in NGC 2320 to stellar and ionized gas kinematics from the longslit spectroscopy of Cretton, Rix, & de Zeeuw (2000). Those authors used the kinematics of [O III], corrected for asymmetric drift, to derive a circular velocity curve for NGC 2320. Figure 14 shows that the total width of the CO line is in very close agreement with the amplitude of the circular velocity curve (assuming the inclination to be 60°). Thus, even though we have not detected a turnover in the CO rotation velocity on the northwest side of the galaxy, we believe that the full width of the CO line is probably a good indicator of the dynamical mass. The quantitative agreement between the circular velocity derived from CO and from [O III] strongly suggests that the bulk of the molecular gas has relaxed into dynamical equilibrium and is now tracing the same gravitational potential that the warm gas traces. Measured [O III] velocities extend to larger radii than the CO gas ($18'' = 7$ kpc) and indicate a dynamical mass of $3.7 \times 10^{11} M_\odot$ within 7 kpc of the center.

The velocity data also suggest that while CO and [O III] may be tracing the same potential, they do not have the same kinematics. The ionized gas has a slower rotation speed and a larger velocity dispersion than the CO. The rotation speed of [O III], corrected for inclination, is 380 km s^{-1} in the flat part of the rotation curve; its velocity dispersion is 200 km s^{-1} in the center of the galaxy and 100 km s^{-1} at $20''$ radius (Cretton, Rix, & de Zeeuw 2000). In contrast, the CO rotation speed at the edge of the molecular disk (also corrected for inclination) is 480 km s^{-1} . The CO velocity dispersion in NGC 2320 cannot be measured directly, but by analogy with 3C31 and Cen A we would expect to find a CO dispersion $\lesssim 20 \text{ km s}^{-1}$ (Okuda et al. 2005; Quillen et al. 1992). Molecular gas could not sustain a velocity dispersion as high as $100\text{--}200 \text{ km s}^{-1}$ without being shocked and destroyed. Of course, it is true that the rotation speed of [O III] could be underestimated by as much as 20% if the major axis slit were offset from the kinematic axis by 20° , but the large number of position angles observed by Cretton, Rix, & de Zeeuw (2000) makes this latter possibility unlikely.

In contrast to NGC 2320, many spiral galaxies show good agreement between ionized and molecular gas kinematics. The Sb galaxy NGC 4527 is a good example (Sofue et al 1999). Lavezzi & Dickey (1998a,b) have also shown that in spirals the CO linewidth is consistent with HI and H α linewidths so that CO spectra can also be used for Tully-Fisher analyses. Such agreement between CO and H α kinematics is reasonable if the ionized gas is in quiescent HII regions which inherited the global rotation velocity and dispersion of the molecular gas from which they formed. But this is apparently not the case in NGC 2320, where the ionized gas has a smaller rotation speed and a larger velocity dispersion than the molecular gas. We conclude that the [O III] in NGC 2320 cannot trace star formation activity. Perhaps the warm ionized gas cooled out of a hot ISM phase; an image of [O III] emission would be useful for testing this hypothesis. NGC 2320 has not apparently been searched deeply for X-ray emission, but its optical luminosity is well up into the range in which O'Sullivan, Forbes, & Ponman (2001) find copious amounts of hot gas.

4.6.3. Angular momentum distribution

Comparisons of cold gas and stellar kinematics are particularly valuable in early type galaxies because such comparisons can test the hypothesis that these galaxies acquired their cold gas from external sources. In NGC 2320 (Figure 14), the maximum rotation velocity of the CO emission is twice that of the stars. Interior to $10'' \sim 3.8$ kpc $\sim r_e/5$, therefore, the specific angular momentum of the gas is twice that of the stars. At face level this result would seem to suggest an external origin for the gas, but the bulk of the stars in the galaxy are beyond $r_e/5$ and we should also consider those more distant stars in the angular momentum comparisons.

We make this analysis of stellar and gaseous angular momenta through a modified version of a procedure outlined by van den Bosch, Burkert & Swaters (2001). Those authors compared the specific angular momentum distribution of the baryons in a galaxy to that of a model dark matter halo as follows. The specific angular momentum $j \equiv rv_\phi(r)$ (v_ϕ is the mean azimuthal velocity) is a monotonically increasing function of radius, as long as v_ϕ does not drop too quickly. (“Too quickly” would have to be faster than a Keplerian decline.) From the mass distribution one may also compute $m(r)$, the mass fraction interior to r , which is also a monotonic function of r . As a result it is straightforward to use the rotation curve to compute $j(r)$ and to construct the cumulative specific angular momentum distribution $m(j)$, a measure of the fractional mass with specific angular momentum less than j . But rather than lumping stars and gas together as van den Bosch, Burkert & Swaters (2001) did, we wish to consider them separately.

The stellar distribution and kinematics of NGC 2320 are taken from Cretton, Rix, & de Zeeuw (2000). Specifically, we assume an oblate spheroid inclined at 60° , the inclination of the gas/dust disk. The stellar density $\rho(R, z)$ is assumed to be the Multi-Gaussian Expansion model of Cretton et al., including five components with dispersions ranging from $0.8''$ to $56''$. We also take the stellar rotation curve, kindly provided in electronic form by N. Cretton, and assume a cylindrical rotation field (the velocity is independent of the distance z from the equatorial plane). This latter assumption may overestimate the stellar angular momenta, but the effect is probably not great since the assumed Gaussian spheroids have 2:1 axis ratios.

For the gas, we make three different models motivated by the facts that (1) the spatial resolution of the CO data is not great and (2) as yet we have no knowledge of the distribution of atomic gas. The first model neglects HI entirely; it assumes that the molecular gas is in a disk of constant surface density. A second model includes HI by presuming that the gas is in an exponential disk whose total mass is twice that of the molecular gas and whose scale length is $5''$. The central surface density in this model equals the observed peak H₂ column density, $370 \text{ M}_\odot \text{ pc}^{-2}$, but the model is too extended in the sense that the gas surface density is still quite high ($50 \text{ M}_\odot \text{ pc}^{-2}$) at the observed edge of the CO disk. A third model has a total mass 1.25 times as large as the H₂ mass and a scale length $3''$. This model has a central surface density of $520 \text{ M}_\odot \text{ pc}^{-2}$. It more accurately reproduces the size and mass of the observed molecular disk; its surface density falls to the present sensitivity limit (3σ in two consecutive channels = $16 \text{ M}_\odot \text{ pc}^{-2}$) at $r = 11''$. All gas is assumed

to follow a rotation curve which rises linearly to a maximum velocity of 480 km s^{-1} at a turnover radius of $5''$ and is flat thereafter, based on Figure 14.

Figure 15 compares the cumulative specific angular momentum distribution for stars and three gas models of NGC 2320. It indicates that the molecular gas has a specific angular momentum well below that of the bulk of the stars; 30–40% of the stellar mass has specific angular momentum greater than the *maximum* value attained by the molecular disk. This result is independent of any assumptions about the distribution of the gas within the disk. It is also independent of any reasonable assumption about the stellar rotation curve beyond its last measured point, which happens to be at $r \sim 30''$ and $j \sim 1820 \text{ kpc km s}^{-1}$ (equal to the maximum angular momentum attained in the molecular disk). When reasonable HI disks are added, it is still true that the median specific angular momentum of the gas (the j value with $m(j) = 0.5$) is less than that of the stars. In fact, only the most extreme HI disk assumed above has a tail of high angular momentum gas which might be inconsistent with the stellar angular momenta.

This analysis suggests that the angular momentum of the molecular gas is actually *consistent* with an origin in stellar mass loss. The mass returning to the ISM would begin, of course, with spatial and angular momentum distributions matching those of the parent stars. The thermal history of the returned mass could be fairly complex, passing through a hot phase (Brighenti & Mathews 1996, 1997). As the gas cooled and settled into a disk it might have contracted, losing a modest fraction of its angular momentum, into the CO disk which is now observed. Future HI observations will help settle the question of whether any atomic gas in NGC 2320 is also consistent with an internal origin.

5. Discussion

5.1. Star formation

The presence of molecular gas naturally suggests the possibility of star formation. Most of the star formation activity in giant ellipticals is supposed to have ended long ago; however, recent UV observations suggest that a trickle of star formation activity may have continued to the present day in some giant ellipticals (Yi et al 2005). Radio continuum and far-IR fluxes can also be useful as star formation indicators (Condon 1992; Wrobel & Heeschen 1988). In this context, we consider radio continuum and FIR fluxes of NGC 83, NGC 2320, and NGC 5838 and ask whether evidence for star formation activity is connected with the presence of molecular gas in these early type galaxies.

Radio continuum flux densities at 1.4 GHz are available for these three galaxies from the NRAO–VLA Sky Survey (Condon et al 1998). IRAS $60\mu\text{m}$ and $100\mu\text{m}$ flux densities are taken from the NASA Extragalactic Database (NED), as updated in 1994 by Knapp. We then calculate a logarithmic FIR/radio flux ratio q as defined by Condon (1992) and others. The vast majority of gas-rich, star forming spiral galaxies have $q \sim 2.34$ with a dispersion of about 0.26 dex (Yun,

Reddy, & Condon 2001) [YRC]. Galaxies whose radio emission is dominated by an active galactic nucleus (AGN) are usually easily identified by their low q values.

Table 4 presents the q values, radio continuum and FIR flux densities for NGC 83, NGC 2320, and NGC 5838. NGC 83 and NGC 5838 lie close to the mean q value of YRC’s sample of star forming galaxies, at 2 and 1 standard deviations in the direction of slight IR excess. Since NGC 83 does contain abundant molecular gas, the most likely source of the radio and FIR fluxes from this galaxy is therefore star formation. The standard interpretation of NGC 5838’s q value would also be star formation, though it is curious that molecular gas has not been reliably detected in NGC 5838.

In contrast, the q value for NGC 2320 is 2.9 standard deviations below the mean. (Miller & Owen (2001) find a similar q value to the one derived here.) According to the definitions of YRC and Condon, Cotton, & Broderick (2002), NGC 2320 is a “radio excess” galaxy meaning that its radio continuum is probably powered by an AGN. That interpretation is consistent with the fact that the radio source in NGC 2320 is still unresolved by the FIRST survey (White et al 1997), so the radio source is much smaller in angular size than the molecular gas distribution. The kinematic data in Section 4.6 also imply that most of the [O III] emission from NGC 2320 is not associated with star formation. Thus, NGC 2320 is rich in molecular gas but there is no conclusive evidence for ongoing star formation activity. NGC 83, also rich in molecular gas, does show evidence for star formation; and NGC 5838, with no detected molecular gas, shows radio continuum and FIR fluxes which would normally be interpreted as star formation. Evidently the connection between molecular gas, star formation, and radio/FIR emission is not as straightforward in early type galaxies as it is in late type galaxies.

Okuda et al. (2005) and Koda et al. (2005) have shown that the molecular surface densities in early type galaxies can be quite high — as high as in starburst galaxies — without inducing detectable star formation. The molecular disks apparently are stabilized by their host galaxies’ large dynamical masses, as one can see from an analysis of Toomre’s Q parameter (Kennicutt 1989). The Q parameter is intended to estimate the degree of gravitational stability of a gas disk in a galaxy, as it is a ratio of the properties which inhibit the growth of gravitational instabilities (local velocity dispersion and epicycle frequency) to the properties which enhance such growth (the gas surface density). Koda et al. (2005) have rewritten Toomre’s Q parameter as $Q \sim \alpha \frac{(M_\sigma M_{dyn})^{1/2}}{M_{gas}}$, where $M_\sigma \equiv R\sigma^2/G$, σ is the local gas velocity dispersion, and α encapsulates the information about the local shape of the rotation curve. When the Q parameter is written in this way it is easy to see that for two galaxies with similar molecular disks (similar R , σ , and M_{gas} or Σ_{gas}), the one with smaller M_{gas}/M_{dyn} has a larger Toomre Q and should have less star formation activity.

In this context, the molecular disks of NGC 83 and NGC 2320 make interesting comparisons with similar disks in 3C 31 (Okuda et al. 2005) and early-type spirals (Koda et al. 2005). As in 3C 31, the molecular surface densities in NGC 83 and NGC 2320 are respectably high; the peak values are $140 \text{ M}_\odot \text{ pc}^{-2}$ and $370 \text{ M}_\odot \text{ pc}^{-2}$, not including helium. The present data do not permit a

meaningful estimate of Toomre’s Q for the molecular disks in NGC 83 and NGC 2320, but it is clear that these galaxies have low ratios of gas to dynamical mass. Specifically, $M_{\text{gas}}/M_{\text{dyn}} \sim 0.03$ in NGC 83 and NGC 2320, similar to the value of 0.02 found in 3C 31 (Okuda et al. 2005). Late-type spirals typically have $M_{\text{gas}}/M_{\text{dyn}} \sim 0.1$ to 1.0 (Koda et al. 2005). Thus the rather low $M_{\text{gas}}/M_{\text{dyn}}$ in NGC 83 and NGC 2320 could provide a plausible explanation for a lack of star formation in these disks.

5.2. Disk growth

Even if star formation does transform the molecular disks into stellar disks, the future stellar disks will not be large or dramatic. The radial extent of the CO emission in NGC 83 and NGC 2320 only corresponds to $\sim 0.2 r_e$ (where r_e is the effective radius or the half-light radius of the de Vaucouleurs $r^{1/4}$ profile). The CO disks in NGC 83 and NGC 2320 are thus smaller, relatively speaking, than the ones in the early type galaxies NGC 807, UGC 1503, NGC 3656, NGC 4476, and NGC 5666 (Young 2002). Those latter five CO disks extended to $0.5\text{--}1 r_e$.

The CO disks in NGC 83 and NGC 2320 are also small when measured as mass fractions of their host galaxies. Cretton, Rix, & de Zeeuw (2000) quote $M_V = -22.5$ for NGC 2320 with a dynamical V -band mass-to-light ratio of 16, which means that the estimated molecular gas mass of $4.3 \times 10^9 M_\odot$ is only 0.3% of the stellar mass. Similarly, if NGC 83 has $M_V = -22.1$ and $(M/L)_V \sim 10$ then its molecular mass ($2.0 \times 10^9 M_\odot$) is only 0.3% of its stellar mass. Star formation might transform CO-rich elliptical galaxies into “two-component disk ellipticals” of the type discussed by Khochfar & Burkert (2004), but any future stellar disks in NGC 83 and NGC 2320 would be significantly smaller in radial extent, less luminous, and more difficult to detect than the embedded stellar disks studied by Scorza & Bender (1995) and Scorza et al. (1998), for example.

On the other hand, the molecular disk in NGC 2320 is *already* associated with an embedded stellar disk. Stellar velocity profiles show that the the Gauss-hermite h_3 parameter is anticorrelated with the mean rotation velocity (Cretton, Rix, & de Zeeuw 2000); this is the classic signature of a dynamically cold disk embedded in a dynamically hot galaxy (van der Marel & Franx 1993). This kinematic disk extends to at least $20''$ and thus is coincident with the bright annulus at $15''$ (Section 4.2). The CO disk in NGC 83 is not, apparently, associated with a stellar disk: in Section 4.1 we found no morphological evidence for an embedded stellar disk beyond the obvious dust disk, though it would be useful to check stellar kinematics of this galaxy. Perhaps, then, the molecular gas in NGC 2320 is a small remnant of a once-larger gas disk which formed the dynamically cold stellar disk. Further insight into this question should come with more detailed mapping of the stellar populations and with an understanding of the origin of the molecular gas.

5.3. The origin of the cold gas

Since the gas and dust in NGC 83 appear so well relaxed, we conclude that *if* they were acquired from an external source it must have been several orbital timescales ago. The orbital timescale at the edge of the CO/dust disk is 3×10^7 – 4×10^7 yr (Section 4.5). The general symmetric appearance of the optical images also suggests that it has been well over a Gyr since NGC 83 experienced any merger, if there was one. Stellar kinematic maps of NGC 83 will be necessary before we can say more about whether the angular momentum distribution of the stars is really inconsistent with that of the gas.

In contrast with NGC 83, the the asymmetries previously noted in the CO distribution of NGC 2320 suggest that not all of the molecular gas in this galaxy is fully relaxed. The general appearance of the gas and dust $10''$ southeast of the nucleus is that of gas which has not yet settled into a relaxed disk (Figure 6 and 13). On the other hand, in the position-velocity diagram (Figure 14) this “extra” gas at 6240 km s^{-1} appears to be a natural turnover in the CO rotation curve. Thus all of the detected CO *could* be relaxed into dynamical equilibrium, but then it is curious that the radial extent and the luminosity of the molecular gas are twice as large on the southeast side of the galaxy as on the northwest side. Regardless of whether the CO emission at 6240 km s^{-1} is interpreted as gas in or out of dynamical equilibrium, we are led to the conclusion that some unusual event must have happened in the core of NGC 2320 a short time ago. The orbital timescale at $10''$ radius and 480 km s^{-1} is only 5×10^7 yr; strong side-to-side asymmetries in the gas distribution should have been smeared out over a few orbital timescales.

The comparisons of the specific angular momentum distributions of gas and stars in NGC 2320 (Section 4.6.3) showed that the presently observed CO disk might conceivably have its origin from internal stellar mass loss. Naturally, such comparisons cannot rule out an external origin, since the angular momentum which is left after a minor or a major merger depends a great deal on the (unknown) geometry of the interaction. Additional studies of larger numbers of CO-rich early type galaxies will be necessary before we can hope to piece together a coherent picture of these fascinating systems.

6. Summary

We present a study of the cold ISM in NGC 83, NGC 2320, and NGC 5838, three early type galaxies selected from single dish CO surveys. Broadband optical imaging of NGC 83 and NGC 2320 gives their optical and dust morphologies. New observations with the BIMA millimeter array give a sensitive CO limit for NGC 5838 as well as the distribution and kinematics of molecular gas in NGC 83 and NGC 2320.

The optical images of NGC 83 and NGC 2320 show classic $r^{1/4}$ surface brightness profiles, lending support to the contention that these are true giant elliptical galaxies rather than misclassified

spirals. In both of these galaxies the CO emission is very closely coincident with internal dust disks (the same is not true for NGC 5838, which also has a dust disk but no detected CO). The kinematic axes of the molecular disks are aligned within a few degrees of the large scale optical major axes, as is also true for most of the early-type galaxies studied by Young (2002). The alignment suggests that these galaxies are probably oblate spheroids.

We also calculate dynamical masses within the outer edge of the CO disks and find that they are consistent with little, if any, dark matter in the interiors of these galaxies; this result is consistent with (but independent of) previous work on stellar kinematics in early-type galaxies.

The CO kinematics also provide clues to the origin of the gas. The kinematics of the CO in NGC 83 suggest that the gas/dust disk is well settled into dynamical equilibrium; if this gas was acquired from an external source, it must have been much longer than about 4×10^7 yr ago. Most of the CO emission and dust in NGC 2320 also appears to be settled into a relaxed disk. CO kinematics in NGC 2320 are consistent with the circular velocity curve inferred by Cretton, Rix, & de Zeeuw (2000) from [O III] emission. However, 25% of the CO is in an asymmetric structure beyond one edge of the disk. This asymmetric structure should be sheared by differential rotation on an orbital timescale of 5×10^7 yr and the short orbital timescale suggests that the gas was acquired or disturbed recently.

We compare the cumulative specific angular momentum distribution of the CO in NGC 2320 to that of the stars. At a given radius (within the CO/dust disk), the rotation velocity of the gas is at least twice the mean velocity of the stars. But since the stars extend so much farther than the CO does, under plausible approximations the specific angular momentum distribution of the cold gas is not inconsistent with that of the stars. From an angular momentum point of view, the molecular gas in NGC 2320 could conceivably have originated in internal stellar mass loss, contraction, and spin-up.

Even though NGC 83 and NGC 2320 are unusually rich (for early-type galaxies) in molecular gas, evidence for star formation activity and stellar disk growth is mixed. For example, the radio and FIR fluxes in NGC 83 suggest possible star formation activity but no unusual structure is noted in the optical morphology. There is a dynamically cold stellar disk or ring in NGC 2320, with the same orientation and a bit larger radial extent than the molecular disk; however, there seems to be little present-day star formation in NGC 2320. The galaxy's radio and FIR fluxes suggest that its radio emission is dominated by an AGN rather than by star formation. Furthermore, the ionized gas in NGC 2320 has significantly higher velocity dispersion and lower rotation velocity than the CO does. That [O III] emission does NOT trace star formation activity in HII regions formed out of the molecular gas; it must have some other energizing source, and perhaps it is cooling out of a hot gas phase. In any case, if the molecular disks in NGC 2320 and NGC 83 do form stellar disks they will be smaller both in relative mass and in radial extent than the ones which are commonly found in disk ellipticals.

Thanks to Tom Statler and Jacqueline van Gorkom for helpful comments and to Liese van Zee for the optical images. Thanks also to the Berkeley-Illinois-Maryland Association (operated with support from the National Science Foundation) for generous investments of telescope time. This work was partially supported by NSF AST-0507423 and it has made use of the NASA/IPAC Extragalactic Database (NED) which is operated by the Jet Propulsion Laboratory, California Institute of Technology, under contract with the National Aeronautics and Space Administration.

Facilities: BIMA, WIYN.

REFERENCES

Akeson, R. 1998, BIMA memo series #68

Brighenti, F., & Mathews, W. G. 1996, ApJ470, 747

Brighenti, F., & Mathews, W. G. 1997, ApJ490, 592

Burstein, D., Davies, R. L., Dressler, A., Faber, S. M., Stone, R. P. S., Lynden-Bell, D., Terlevich, R. J., & Wegner, G. 1987, ApJS, 64, 601

Charmandaris, V., Combes, F., & van der Hulst, J. M. 2000, A&A, 356, L1

Ciotti, L., & Bertin, G. 1999, A&A, 352, 447

Ciotti, L., Pellegrini, S., Renzini, A., & D'Ercole, A. 1991, ApJ, 376, 380

Combes, F., Bureau, M., Young, L. M., & van Gorkom, J. H. 2005, in preparation

Condon, J. J. 1992 ARAA 30, 575

Condon, J. J., Cotton, W. D., Greisen, E. W., Yin, Q. F., Perley, R. A., Taylor, G. B., & Broderick, J. J. 1998, AJ, 115, 1693

Condon, J. J., Cotton, W. D., & Broderick, J. J. 2002, AJ 124, 675

Cretton, N., Rix, H.-W., & de Zeeuw, P. T. 2000, ApJ, 536, 319

Dehnen, W. 1993, MNRAS 265, 250

de Vaucouleurs, G., de Vaucouleurs, A., Corwin Jr., H.G., Buta, R. J., Paturel, G., & Fouque, P. 1991, Third Reference Catalogue of Bright Galaxies, Version 3.9

de Zeeuw, P. T., et al. 2002, MNRAS, 329, 513

de Zeeuw, T., & Franx, M. 1989, ApJ, 343, 617

Donzelli, C. J. & Davoust, E. 2003 A&A, 409, 91

Faber, S. M. & Gallagher, J. S. 1976, ApJ, 204, 365

Falcón-Barroso, J., Balcells, M., Peletier, R. F., & Vazdekis, A. 2003, A&A, 405, 455

Guelin, M., Kramer, C., & Wild, W. 1995, IRAM Newsletter, 20 January 1995

Hatch, N. A., Crawford, C. S., Fabian, A. C., & Johnstone, R. M. 2005, MNRAS in press (astro-ph/0411446)

Huchra, J. P., Vogeley, M. S., & Geller, M. J. 1999, ApJS, 121, 287

Inoue, M. Y., Kameno, S., Kawabe, R., Inoue, M., Hasegawa, T., & Tanaka, M. 1996, AJ, 111, 1852

Kennicutt, R. C. 1989, ApJ, 344, 685

Khochfar, S., & Burkert, A. 2004, MNRAS, submitted (astro-ph/0409705)

Knapp, G. R., Guhathakurta, P., Kim, D., & Jura, M. A. 1989, ApJS, 70, 329

Knapp, G. R. & Rupen, M. P. 1996, ApJ, 460, 271

Koda, J., Okuda, T., Nakanishi, K., Kohno, K., Ishizuki, S., Kuno, N., & Okumura, S. K. 2005, A&A, in press (astro-ph/0412274)

Kuntschner, H., Lucey, J. R., Smith, R. J., Hudson, M. J., & Davies, R. L. 2001, MNRAS, 323, 615

Lavezzi, T. E., & Dickey, J. M. 1998, AJ 115, 405

Lavezzi, T. E., & Dickey, J. M. 1998, AJ 116, 2672

Lay, O. 1999, BIMA memo series # 72

Lees, J. F., Knapp, G. R., Rupen, M. P., & Phillips, T. G. 1991, ApJ, 379, 177

Michard, R., & Marchal, J. 1994, A&AS, 105, 481

Miller, N. A., & Owen, F. N. 2001 ApJS 134, 355

Nieto, J.-L., Poulain, P., Davoust, E., & Rosenblatt, P. 1991, A&AS, 88, 559

Okuda, T., Kohno, K., Iguchi, S., & Nakanishi, K. 2005, ApJ, 620, 673

O’Sullivan, E., Forbes, D. A., & Ponman, T. J. 2001, MNRAS 328, 461

Peletier, R. F., Balcells, M., Davies, R. L., Andredakis, Y., Vazdekis, A., Burkert, A., & Prada, F. 1999, MNRAS, 310, 703

Quillen, A. C., de Zeeuw, P. T., Phinney, E. S., & Phillips, T. G. 1992, ApJ, 391, 121

Ravindranath, S., Ho, L. C., Peng, C. Y., Filippenko, A. V., & Sargent, W. L. W. 2001, AJ, 122, 653

Regan, M. W., Thornley, M. D., Helfer, T. T., Sheth, K., Wong, T., Vogel, S. N., Blitz, L., & Bock, D. C.-J. 2001, ApJ, 561, 218

Rupen, M. P. 1997, in The Nature of Elliptical Galaxies (ASP Conference Series 116), eds. M. Arnaboldi, G. S. da Costa, & P. Saha

Sandage, A., & Bedke, J. 1994, The Carnegie Atlas of Galaxies (Washington, DC: Carnegie Institution of Washington with The Flintridge Foundation)

Sault, R. J., Teuben, P. J., & Wright, M. C. H. 1995, in ASP Conf. Ser. 77, Astronomical Data Analysis Software and Systems IV, ed. R. A. Shaw, H. E. Payne, & J. J. E. Hayes (San Francisco: ASP), 433

Schlegel, D. J., Finkbeiner, D. P., & Davis, M. 1998, ApJ, 500, 525

Scorza, C., Bender, R., Winkelmann, C., Capaccioli, M., & Macchetto, D. F. 1998, A&AS, 131, 265

Scorza, C., & Bender, R. 1995, A&A, 293, 20

Smith et al. 2000, MNRAS313, 469

Sofue, Y., Tomita, A., Honma, M., & Tutui, Y. 1999, PASJ 51, 737

Trager, S. C., Worthey, G., Faber, S. M., Burstein, D., & González, J. J. 1998, ApJS, 116, 1

van den Bosch, F. C., Burkert, A., & Swaters, R. A. 2001, MNRAS, 326, 1205

van der Marel, Roeland P., & Franx, M. 1993, ApJ, 407, 525

van Zee, L., Barton, E. J., & Skillman, E. D. 2004, AJ, 128, 2797

Welch, W. J. et al. 1996, PASP, 108, 93

Wiklind, T., Combes, F., & Henkel, C. 1995, A&A, 297, 643 (WCH95)

White, R. L., Becker, R. H., Helfand, D. J., & Gregg, M. D. 1997, ApJ 475, 479

Wiklind, T., Combes, F., Henkel, C., & Wyrowski, F. 1997, A&A, 323, 727

Wong, T. 2001, Ph.D. thesis, University of California at Berkeley.

Wrobel, J. M. & Heeschen, D. S. 1988, ApJ 335, 677

Yi, S. K., Yoon, S.-J., Kaviraj, S., et al. 2005, ApJ619, 111

Young, L. M. 2002, AJ124, 788

Yun, M. S., Reddy, N. A., & Condon, J. J. 2001 ApJ 554, 803

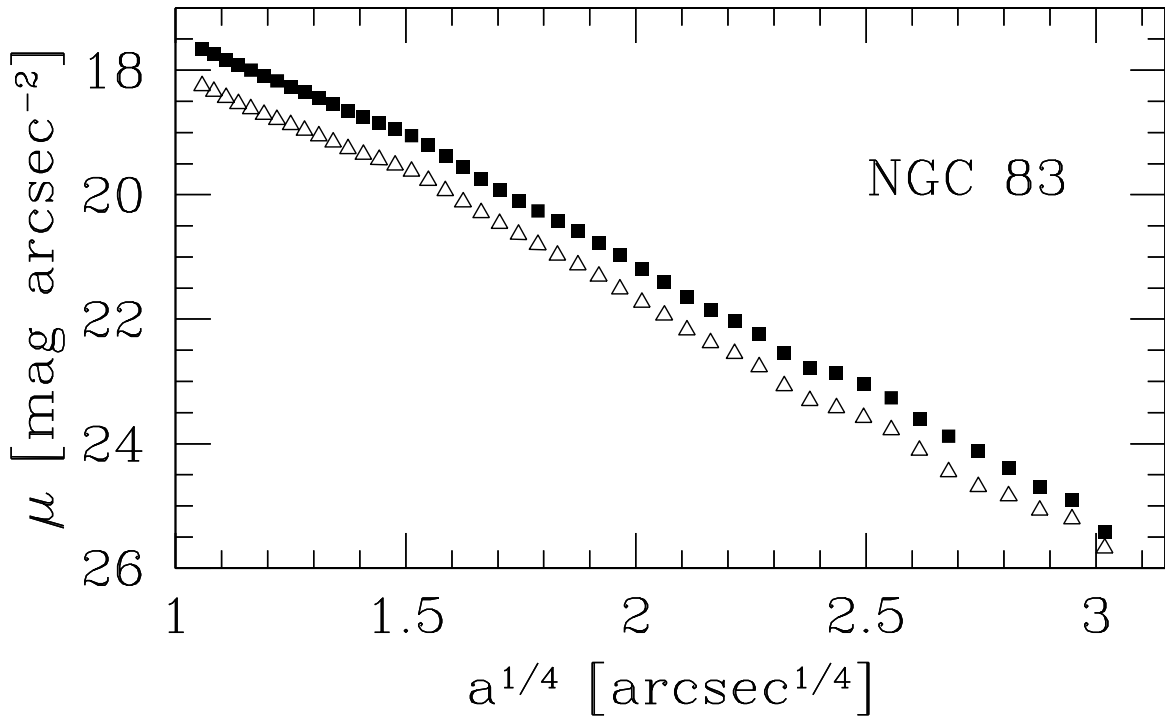


Fig. 1.— Surface brightness profiles of NGC 83. R is in filled squares and V is in open triangles. The break in slope at $a^{1/4} \sim 1.5$ arcsec $^{1/4}$ is due to the dust disk. Approximate flux calibration for these profiles is derived by matching the photometry in circular apertures to data in the hyperLEDA database; it is estimated to be accurate to ± 0.05 mag. Corrections for Galactic extinction are also applied, amounting to 0.23 magnitudes in V and 0.185 mag in R (Schlegel, Finkbeiner, & Davis 1998).

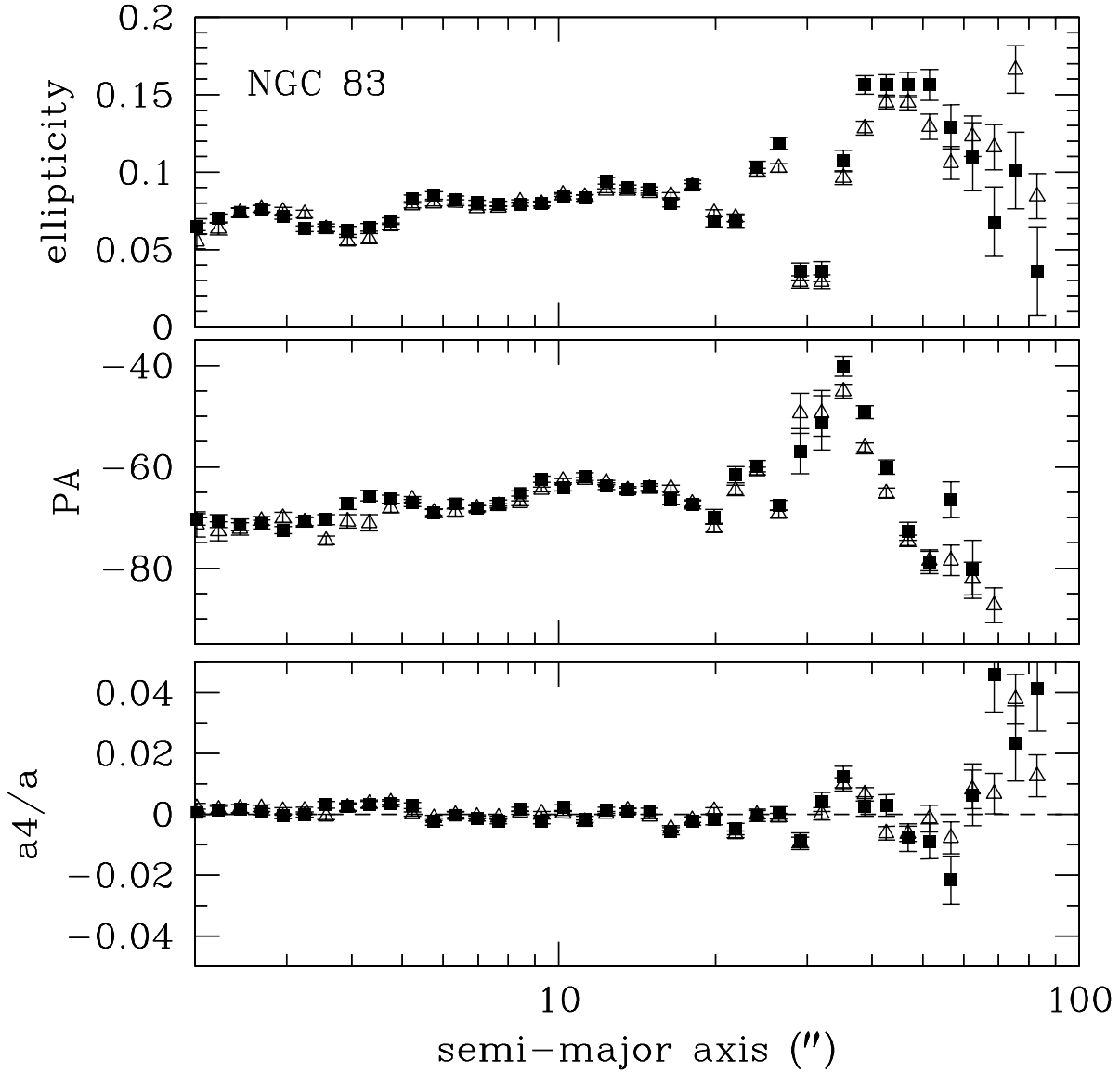


Fig. 2.— Optical morphology of NGC 83. The isophote ellipticity, position angle, and deviations from pure ellipses (a_4/a) are indicated for the R image (filled squares) and the V image (open triangles). Fitted parameters at $a \leq 5''$ are affected by dust.

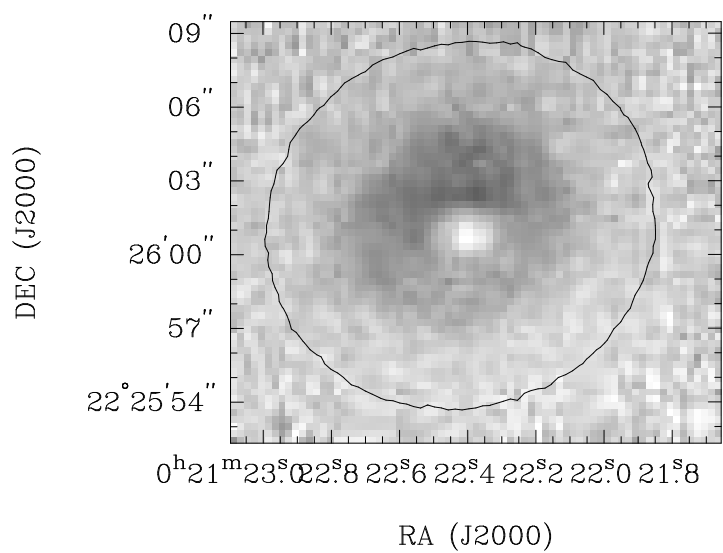


Fig. 3.— $V - R$ color in NGC 83. Darker pixels have redder $V - R$ colors. An isophote from the R image is superposed.

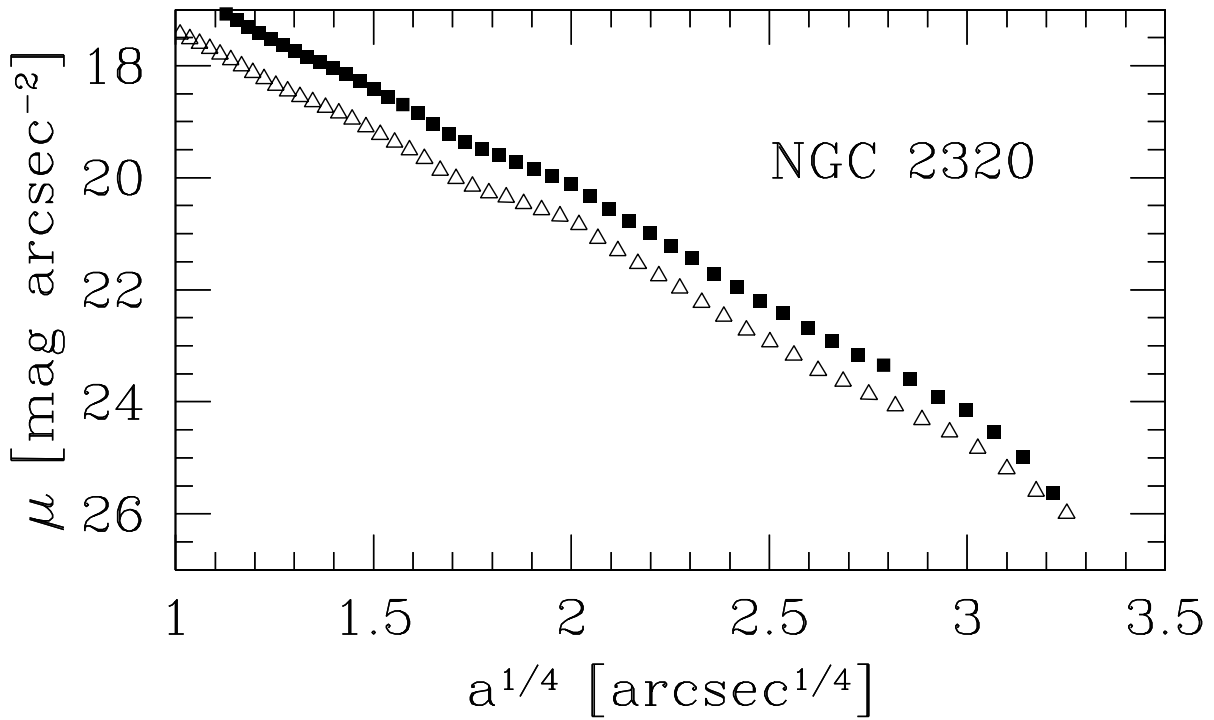


Fig. 4.— Surface brightness profiles of NGC 2320. Dust extinction is visible at radii $\leq 12''$. As for Figure 1, the surface brightness profiles were roughly calibrated with circular aperture photometry from the hyperLEDA database. Galactic extinctions of 0.226 mag (V ; triangles) and 0.182 mag (R ; squares) were applied (Schlegel, Finkbeiner, & Davis 1998).

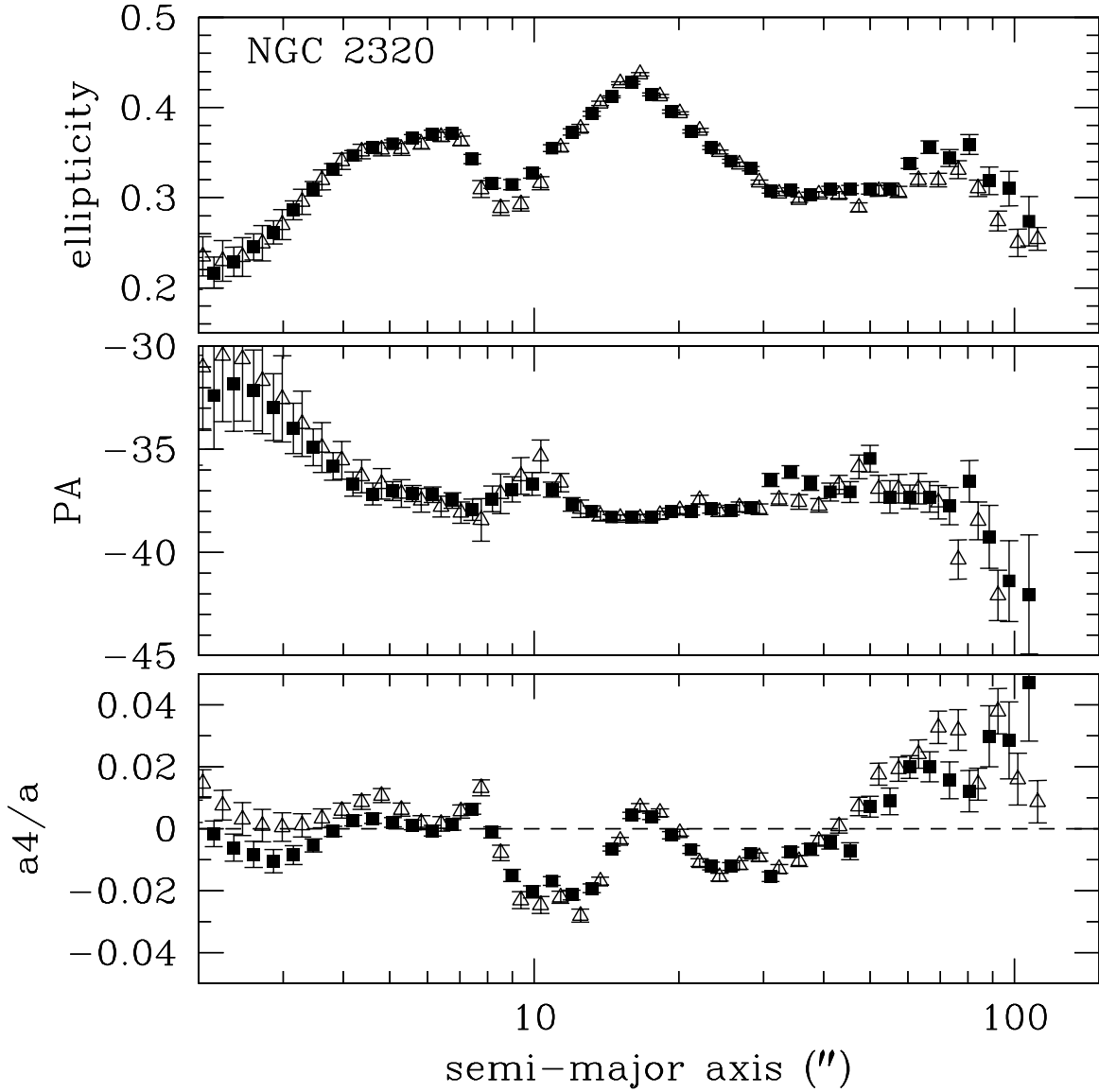


Fig. 5.— Optical morphology of NGC 2320. The isophote ellipticity, position angle, and deviations from pure ellipses (a_4/a) are indicated for the *R* image (filled squares) and the *V* image (open triangles). Fitted parameters at $a \leq 12''$ are affected by dust.

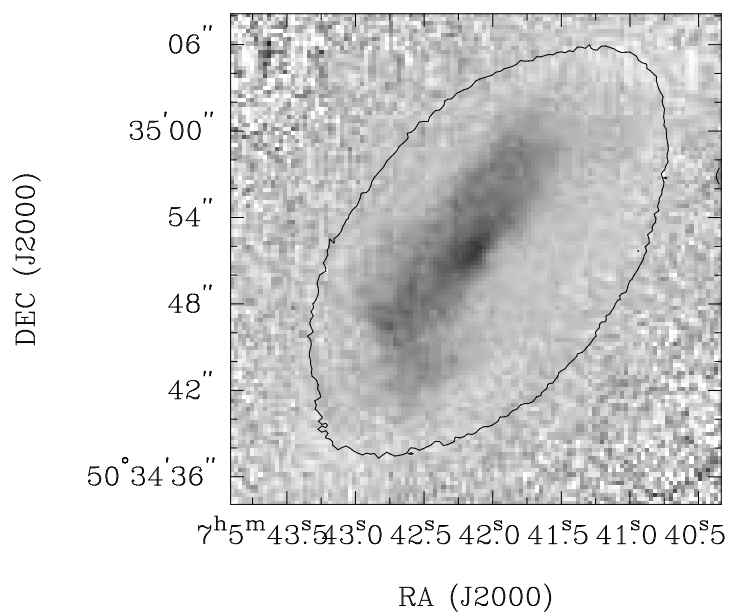


Fig. 6.— $V - R$ color in NGC 2320. Darker pixels have redder $V - R$ colors. An isophote from the R image is superposed.

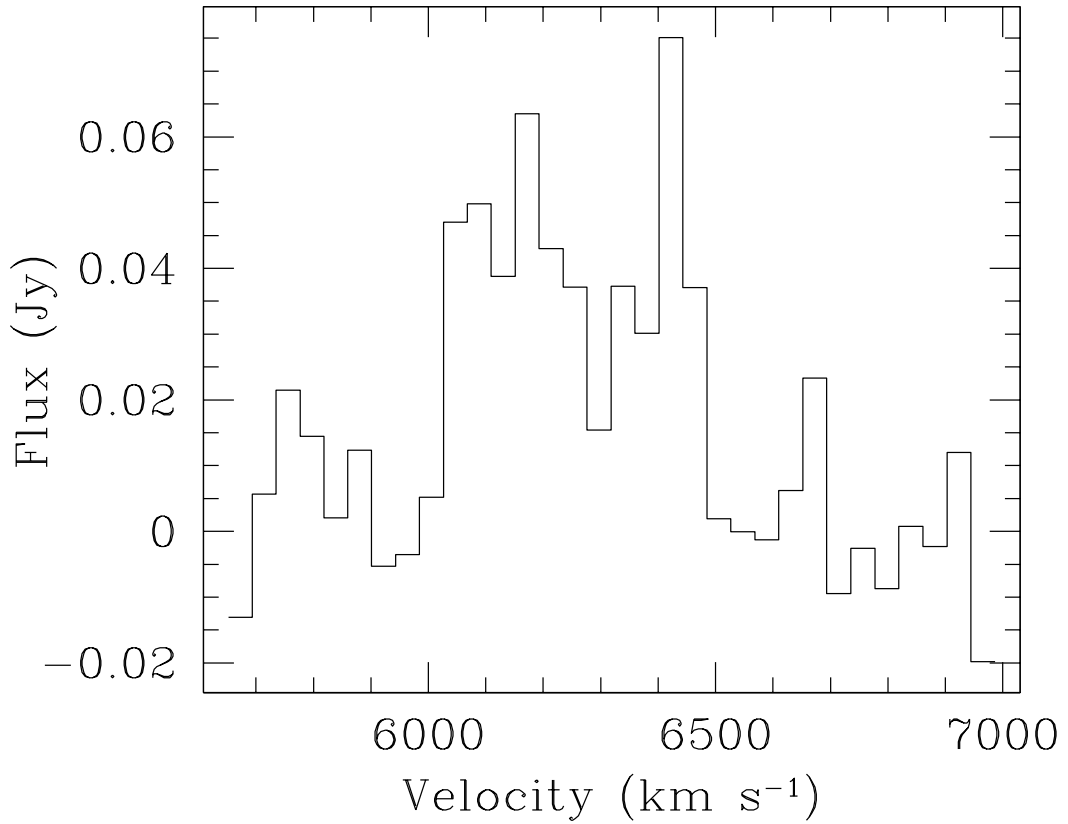


Fig. 7.— CO spectrum of NGC 83. The spectrum was constructed by first using the integrated intensity image (Figure 9) to define an irregular mask region within which the emission is located. The intensity was integrated over the same spatial region for every channel, so the noise in the line-free regions of the spectrum should be indicative of the noise on the line as well.

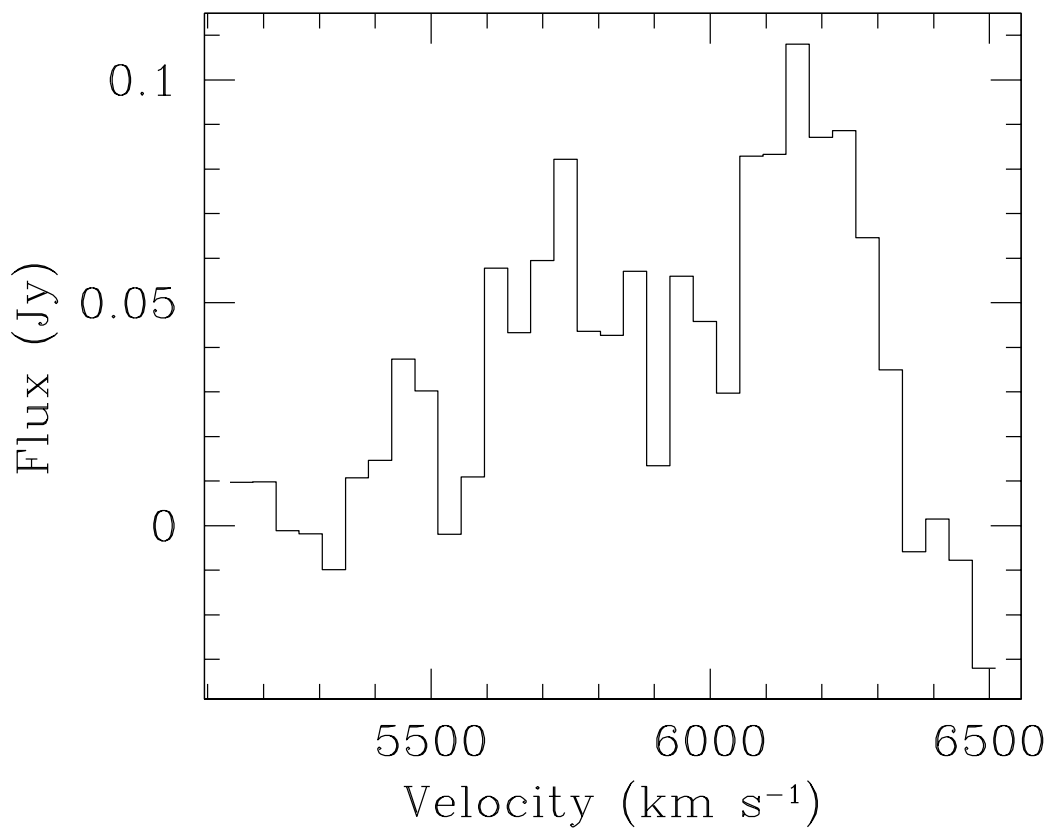


Fig. 8.— CO spectrum of NGC 2320. The spectrum was constructed in the same way as Figure 7.

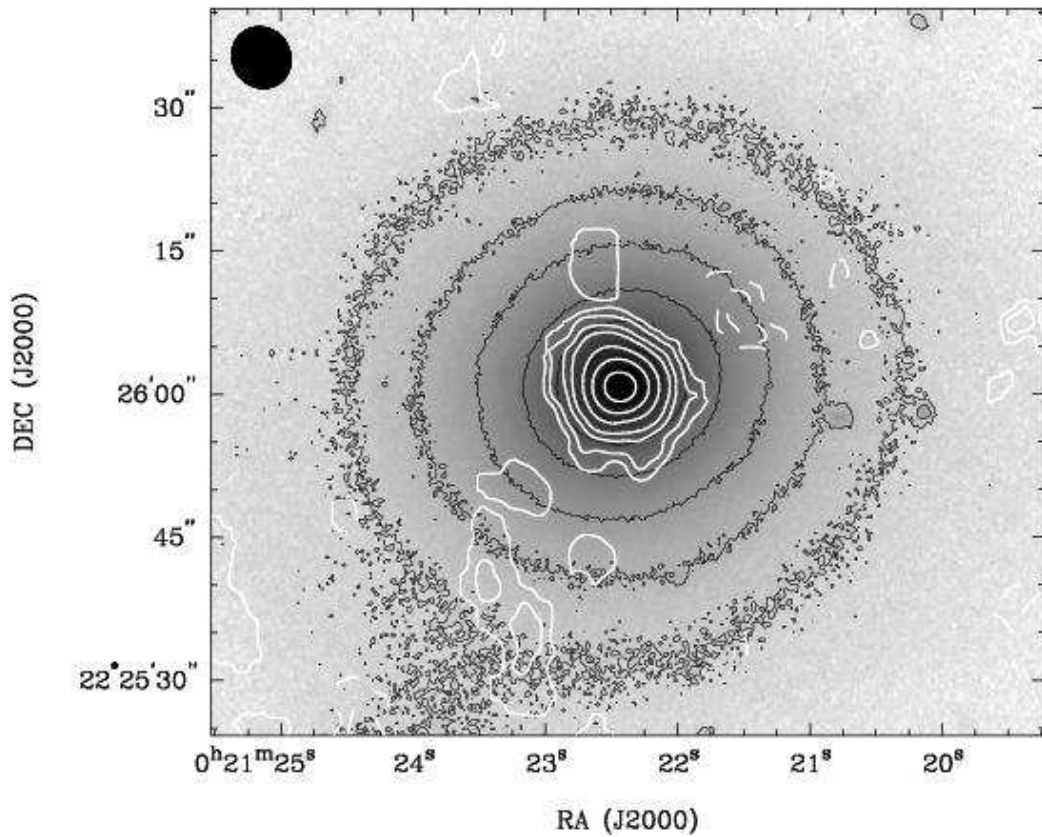


Fig. 9.— Optical and CO images of NGC 83. The greyscale is the WIYN 3.5m *R* image; black contours are optical isophotes separated by a factor of 2. White contours are the integrated CO intensity map. CO contour levels are $-10, -5, 5, 10, 20, 30, 50, 70$, and 90 percent of the peak ($12.7 \text{ Jy b}^{-1} \text{ km s}^{-1}$, or $8.8 \times 10^{21} \text{ cm}^{-2}$).

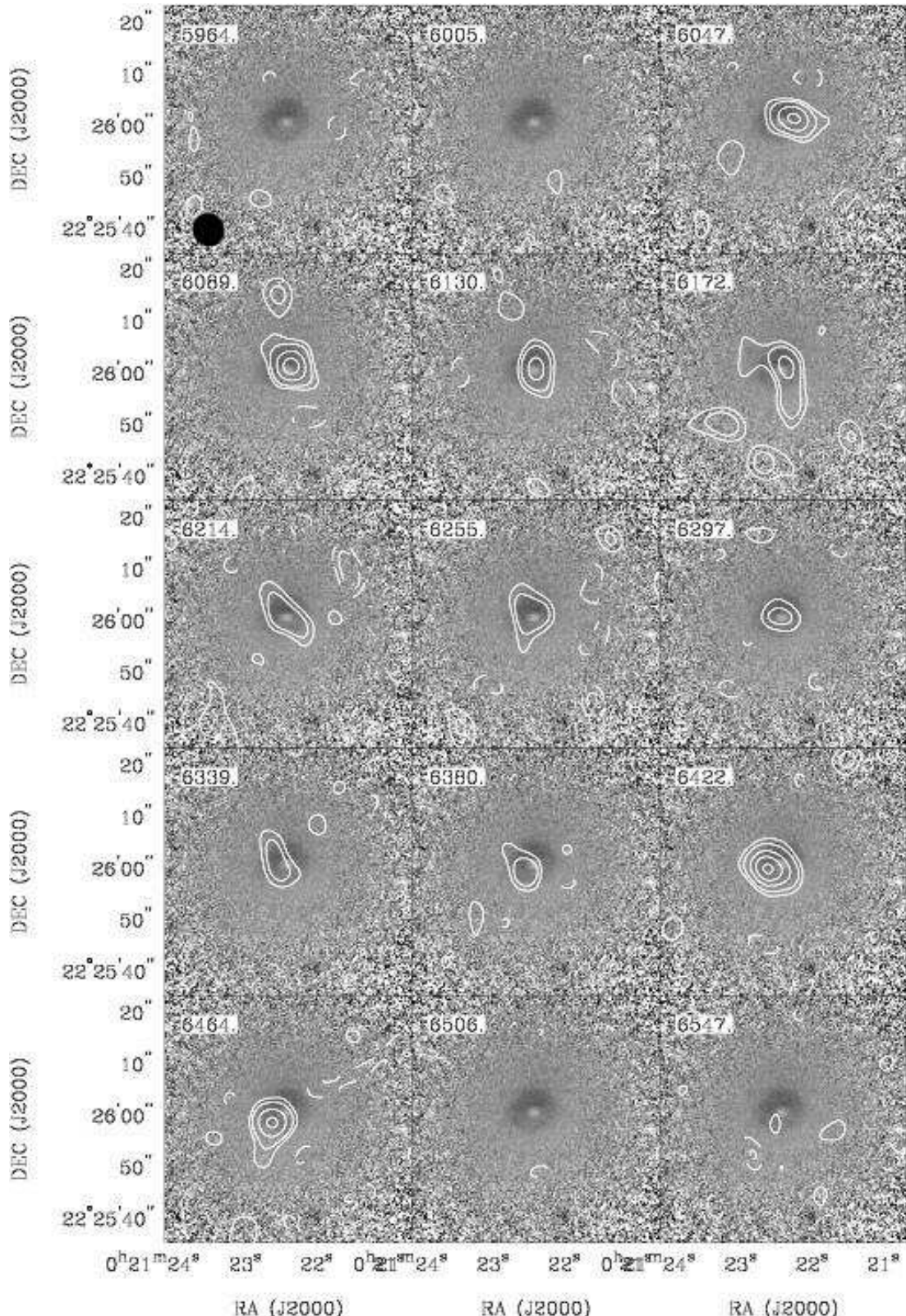


Fig. 10.— Individual channel maps showing CO emission from NGC 83. Contour levels are $-3, -2, 2, 3, 5, 7$, and 9 times $5.8 \text{ mJy beam}^{-1} = 1\sigma$. The greyscale is the $V - R$ image. The velocity of each channel (in km s^{-1}) is indicated in the upper left corner, and the beam size is shown in the bottom left corner of the first channel. The peak CO intensity at $6.6'' \times 6.0''$ resolution is $55 \text{ mJy beam}^{-1} = 130 \text{ mK}$.

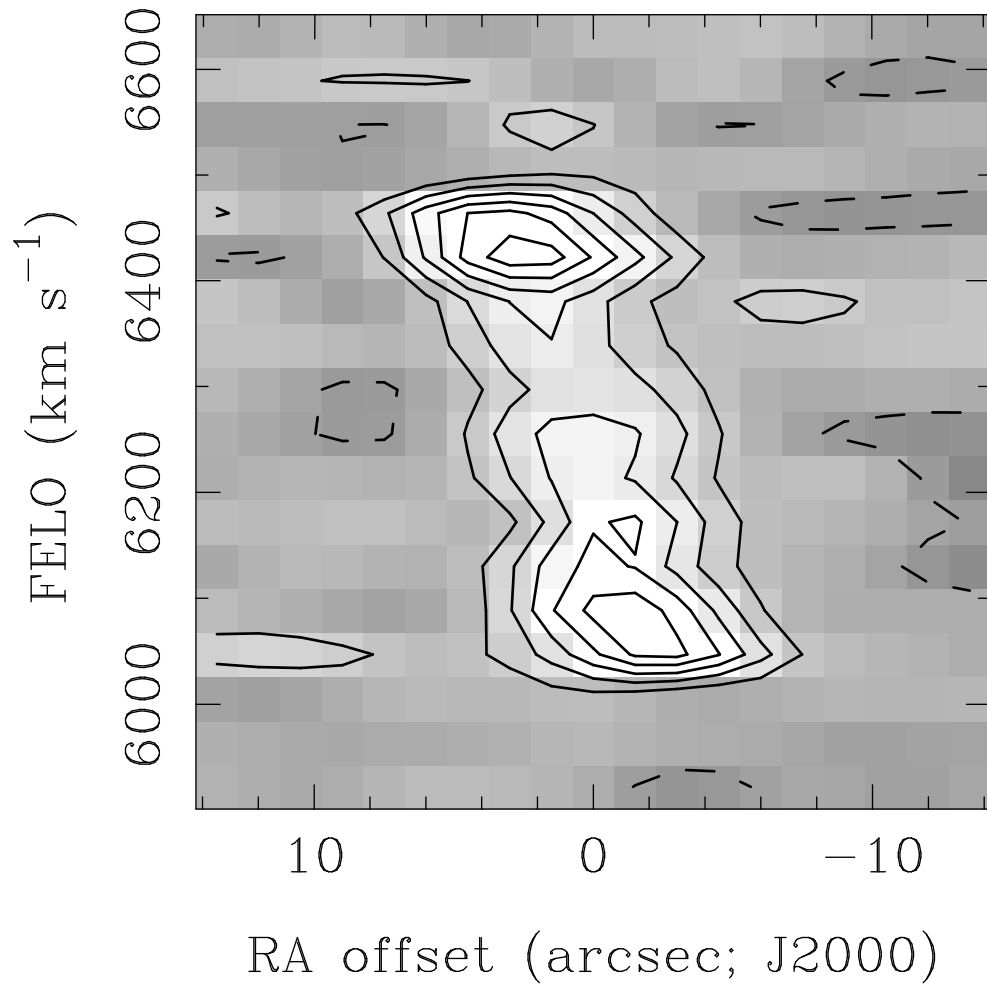


Fig. 11.— Major axis position-velocity diagram for CO in NGC 83. Contours indicate the intensity at -15, 15, 30, 45, 60, 75, and 90 percent of the peak (51 mJy beam⁻¹).

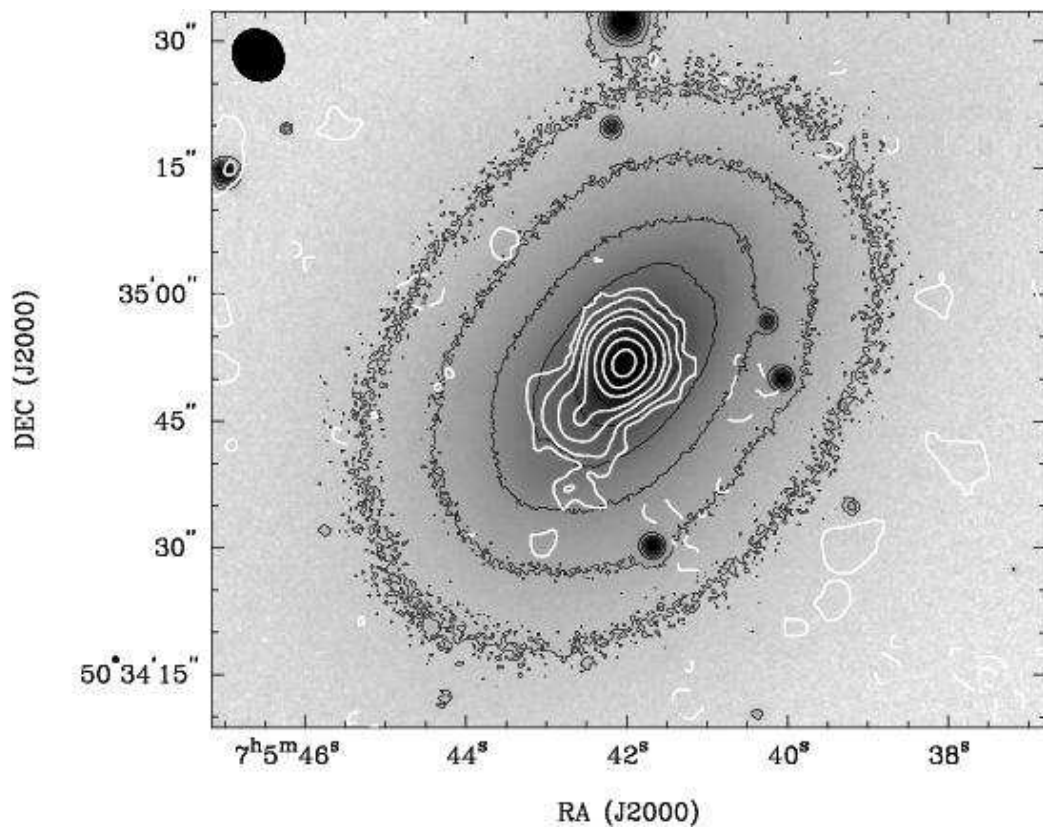


Fig. 12.— Optical and CO images of NGC 2320. The greyscale is the WIYN 3.5m R image; black contours are optical isophotes separated by a factor of 2. White contours are the integrated CO intensity map. CO contour levels are $-10, -5, 5, 10, 20, 30, 50, 70$, and 90 percent of the peak ($30.4 \text{ Jy b}^{-1} \text{ km s}^{-1}$, or $2.3 \times 10^{22} \text{ cm}^{-2}$).

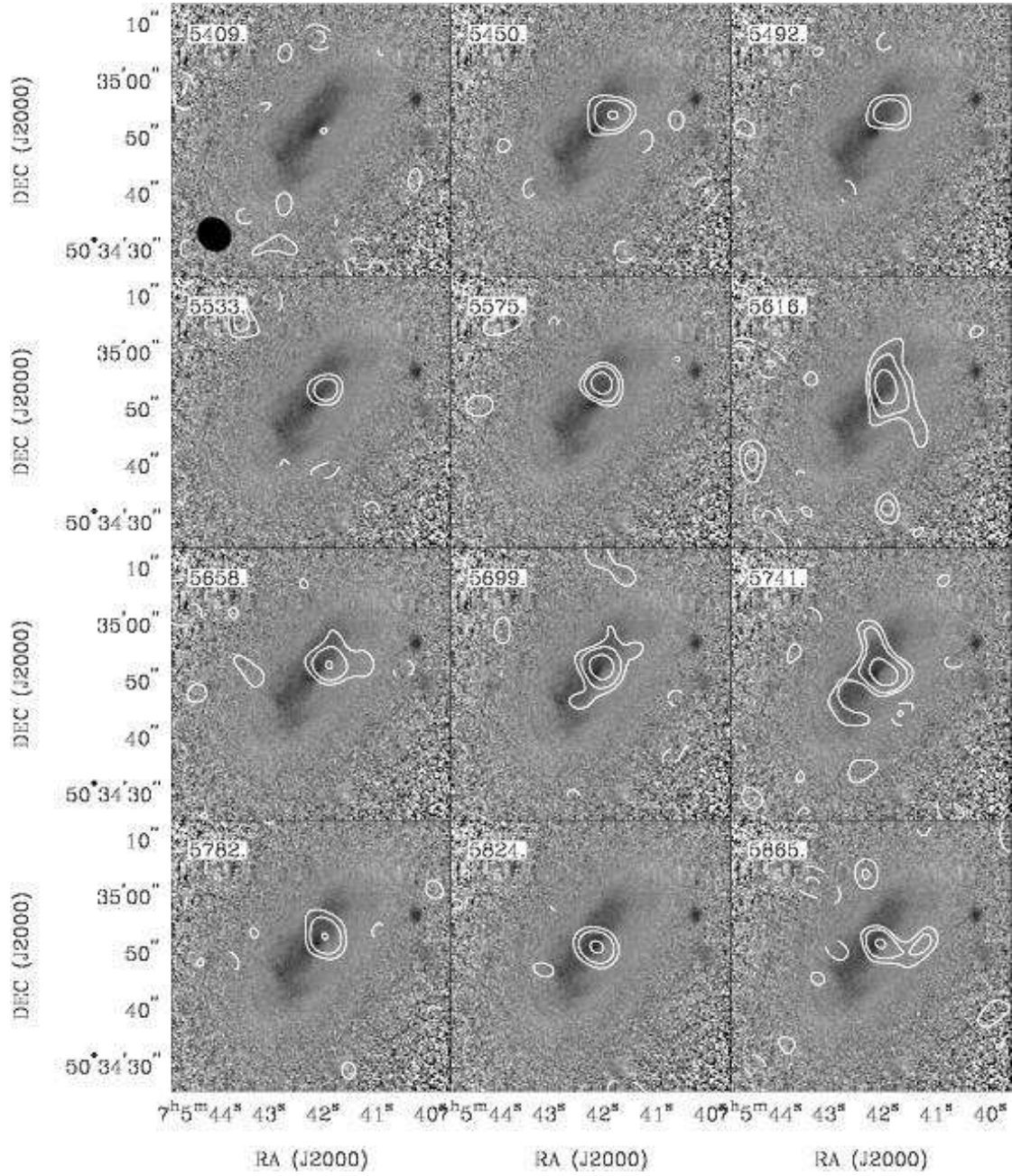


Fig. 13.— Individual channel maps showing CO emission from NGC 2320. Symbols and contour intervals are the same as for Figure 10 but the multiplicative unit is $1\sigma = 7.5 \text{ mJy beam}^{-1}$. The greyscale is the $V - R$ image. The peak CO intensity at $6.4'' \times 5.6''$ resolution is $61 \text{ mJy beam}^{-1} = 150 \text{ mK}$.

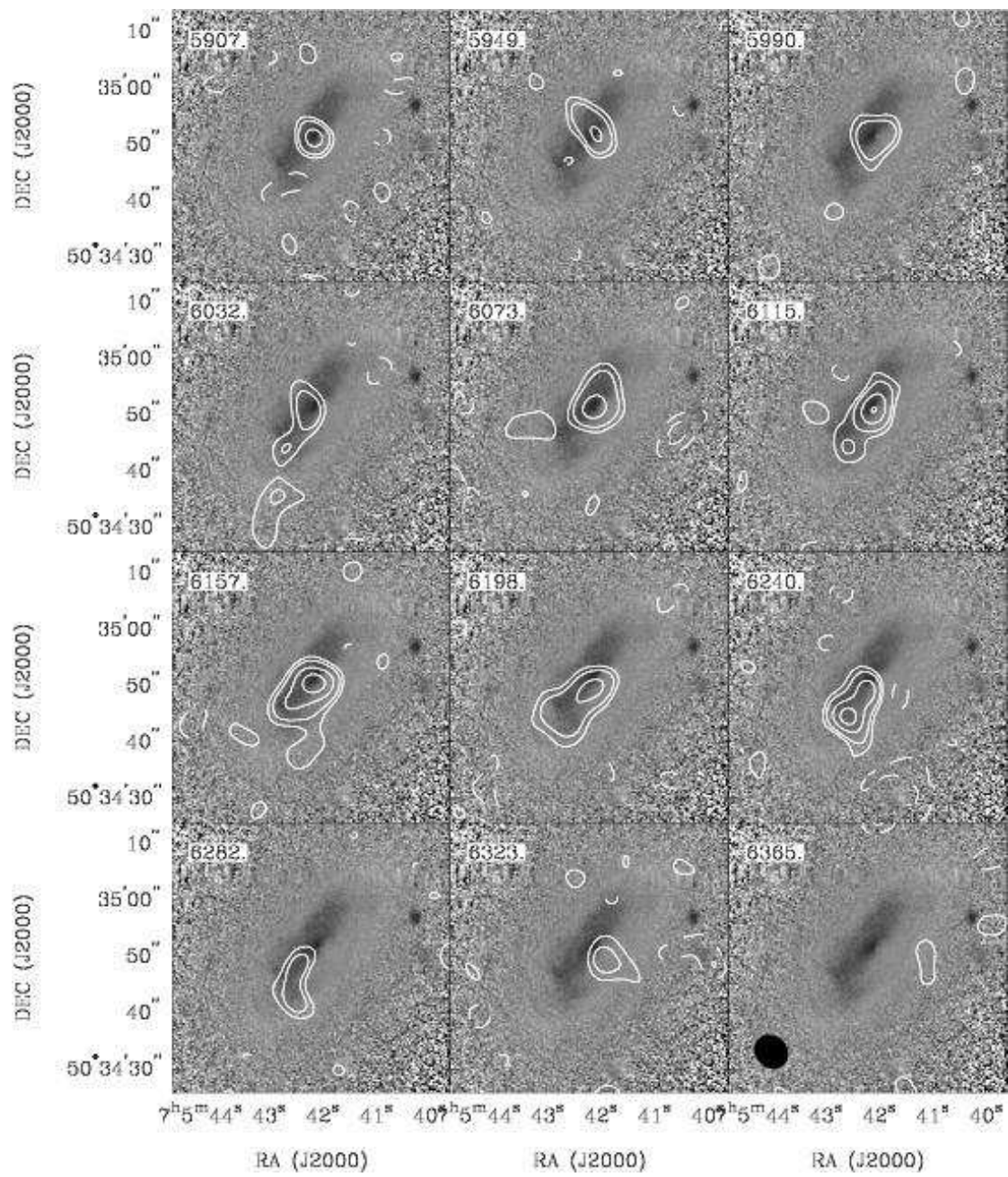


Fig. 13.— Channel maps for NGC 2320, continued from Figure 13.

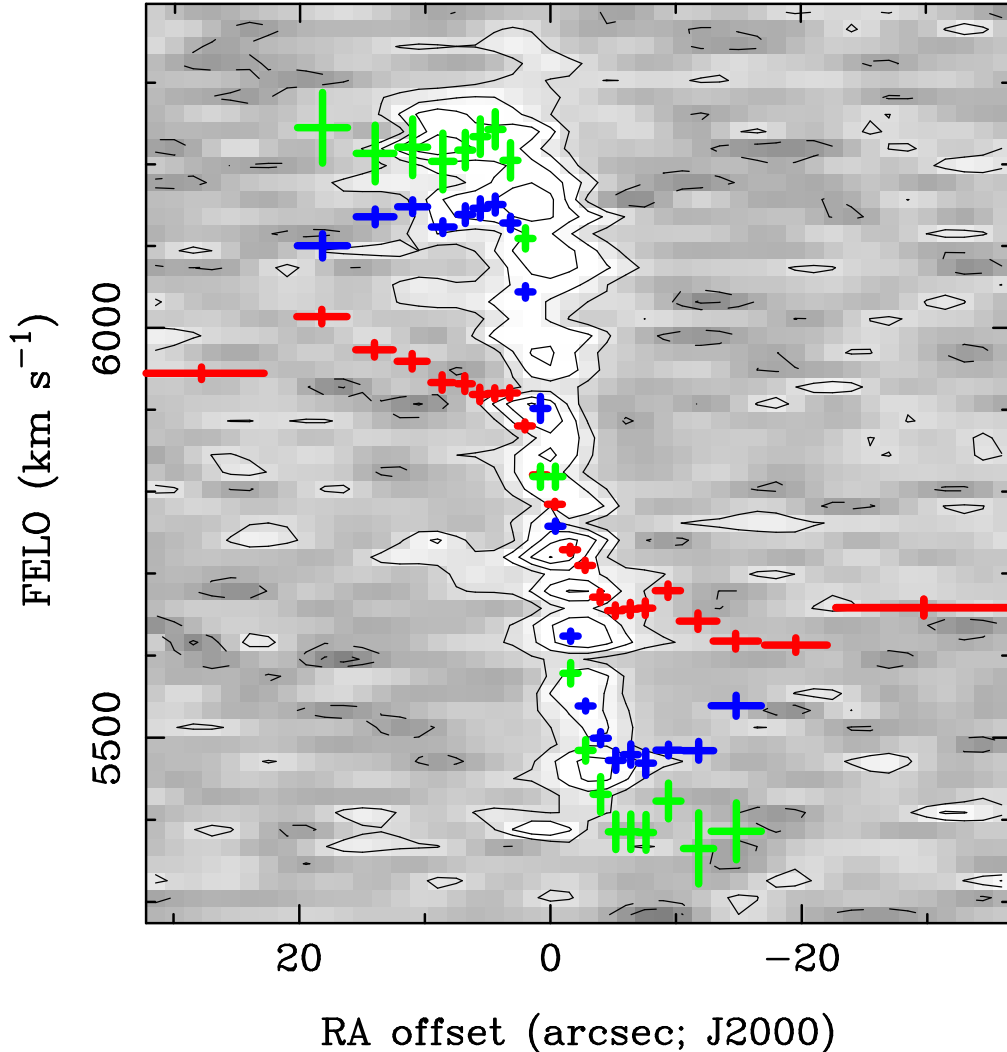


Fig. 14.— NGC 2320 major axis position-velocity diagram. Greyscale and contours show the CO intensity at -20, 20, 40, 60, and 80 percent of the peak (64 mJy beam^{-1}). The solid line (red crosses in the electronic edition) indicates velocities measured from the stellar absorption line data of Cretton, Rix, & de Zeeuw (2000). The dotted line (blue crosses) indicates [OIII] velocities from the same source. All of these are uncorrected for inclination, i.e. they are $V \sin i$. The long-dash line (green crosses) indicates the circular velocity curve derived by Cretton et al. by correcting the [OIII] velocities for inclination and asymmetric drift. Here we have multiplied the circular velocities by $(\sin i)$ in order to compare with the observed CO kinematics. In the limit that the velocity dispersion of the molecular gas is very small and the CO has relaxed into dynamical equilibrium, the CO emission is expected to follow the circular velocity curve.

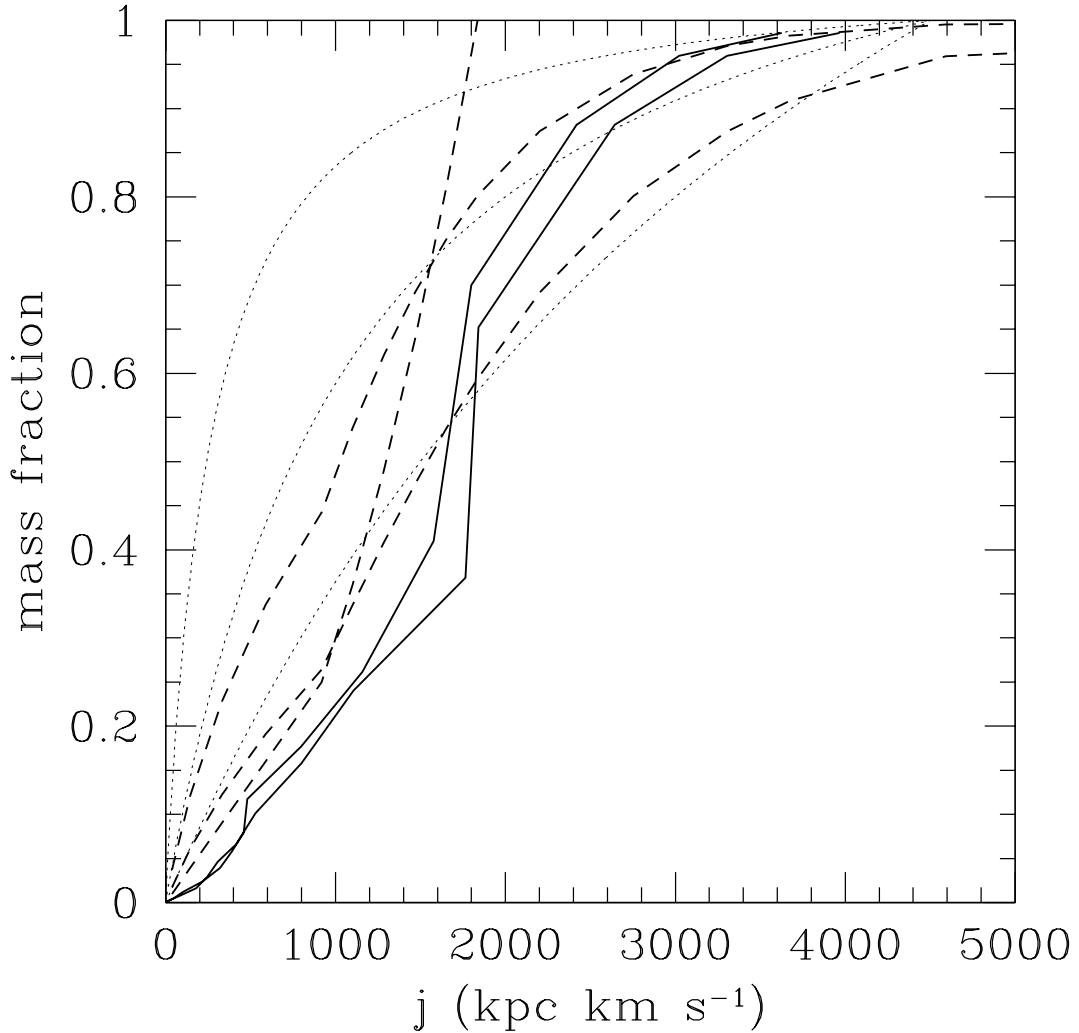


Fig. 15.— Cumulative specific angular momenta of gas and stars in NGC 2320. The vertical axis plots the mass fraction $m(j)$ with specific angular momentum less than j . Two heavy solid lines show $m(j)$ calculated as described in the text for the stellar rotation (both sides of the major axis are plotted). The difference between the two solid lines is an indicator of the uncertainty introduced by errors in the stellar velocities. Three heavy dashed lines show $m(j)$ for the cold gas in the galaxy; the model which includes only H₂ reaches $m(j) = 1$ at the edge of the observed CO disk where $j = 1800 \text{ kpc km s}^{-1}$. The other two dashed lines include hypothetical extended atomic hydrogen disks. For comparison, three light dotted lines show the angular momentum distributions of Λ CDM dark matter halos as in van den Bosch, Burkert & Swaters (2001). A maximum specific angular momentum $j_{max} = 4500 \text{ kpc km s}^{-1}$ is assumed for these dark matter halos.

Table 1. Sample Galaxies – Optical Properties

	NGC 83	NGC 2320	NGC 5838
RA (J2000.0)	00 21 22.4	07 05 42.0	15 05 26.2
Dec	+22 26 01	+50 34 52	+02 05 58
Velocity (km s ⁻¹)	6359 (27)	5944 (15)	1359 (10)
Distance (Mpc)	85	79	18.7
M_B	−21.1	−21.5	−19.6
($B - V$) _e	1.12	1.05	1.02
σ_0 (km s ⁻¹)	250	350	266
r_e (")	27	43	...
r_e (kpc)	11	16	...

Note. — Velocities and blue magnitudes are taken from the NASA Extragalactic Database (NED). The distance estimates for NGC 83 and NGC 2320 are taken from WCH95, who used $H_0 = 75$ km s^{−1} Mpc^{−1} and a Virgocentric infall model. The distance for NGC 5838 is from de Zeeuw et al. (2002). Colors and velocity dispersions are from the hyperLEDA database; effective radii are from Burstein et al. (1987).

Table 2. CO Observation Parameters

Galaxy	Flux cal	Phase cal	Velocity Range km s ^{−1}	FOV kpc	3mm cont. mJy
NGC 83	Uranus, 3C454.3	3C454.3	5673–6986	41	< 5.1
NGC 2320	Mars	0646+448, 0533+483, 0753+538	5160–6490	38	< 13.5
NGC 5838	Mars	1550+054	669–1960	9	< 8.1

Note. — Field of view (FOV) is the FWHM of the primary beam (100") at the distances in Table 1.

Table 3. CO Image Properties

Galaxy	Beam ''	Beam kpc	Channel km s ⁻¹	noise mJy beam ⁻¹	N(H ₂) limit 10 ²⁰ cm ⁻²
NGC 83	6.6×6.0	2.7×2.5	20.9	7.7	3.3
	6.6×6.0	2.7×2.5	41.7	5.8	5.1
	10.1×9.7	4.2×4.0	41.7	7.4	2.6
NGC 2320	6.4×5.6	2.4×2.2	20.8	9.9	4.7
	6.4×5.6	2.4×2.2	41.6	7.5	7.1
	9.8×9.4	3.7×3.6	41.6	9.8	3.7
NGC 5838	8.1×6.0	0.83×0.55	20.2	19	6.5
	11.3×10.0	1.0×0.9	40.3	17	4.9

Note. — The N(H₂) limit is a sensitivity estimate corresponding to a 3 σ signal in one channel.

Table 4. FIR and Radio Continuum Emission

	NGC 83	NGC 2320	NGC 5838
$S_{100\mu\text{m}}$, Jy	2.15±0.18	1.60±0.10	1.67±0.09
$S_{60\mu\text{m}}$, Jy	0.34±0.09	0.26±0.02	0.73±0.04
$S_{1.4GHz}$, mJy	< 1.5	19.3±0.7	2.6±0.4
q	> 2.83	1.60±0.03	2.66±0.07